RosetteArray® Platform for Quantitative High-Throughput Screening of Human Neurodevelopmental Risk

Brady F. Lundin[1,2,3,*], Gavin T. Knight[3,4,*], Nikolai J. Fedorchak[4], Kevin Krucki[4], Nisha Iyer[1,3], Jack E. Maher[3], Nicholas R. Izban[3], Abilene Roberts[3], Madeline R. Cicero[3], Joshua F. Robinson[5], Bermans J. Iskandar[6], Rebecca Willett[4,7], and Randolph S. Ashton[1,3,4,8]

[1]Department of Biomedical Engineering, University of Wisconsin-Madison, Madison, WI 53705, USA
[2]Medical Scientist Training Program, University of Wisconsin-Madison, School of Medicine and Public Health, Madison, WI, 53705 USA
[3]Wisconsin Institute for Discovery, University of Wisconsin-Madison, Madison, WI 53715, USA
[4]Neurosetta LLC, 330 N. Orchard Street Rm 4140A, Madison, WI 53715 USA
[5]Center of Reproductive Sciences, Department of Obstetrics, Gynecology and Reproductive Sciences, University of California, San Francisco, San Francisco, CA 94143, USA
[6]Department of Neurological Surgery, University of Wisconsin-Madison, School of Medicine and Public Health, Madison, WI 53705, USA
[7]Departments of Statistics and Computer Science, University of Chicago, Chicago, IL 60637, USA
[8]Lead Contact, correspondence: rashton2@wisc.edu

*Equal contribution

SUMMARY

Neural organoids have revolutionized how human neurodevelopmental disorders (NDDs) are studied. Yet, their utility for screening complex NDD etiologies and in drug discovery is limited by a lack of scalable and quantifiable derivation formats. Here, we describe the RosetteArray platform's ability to be used as an off-the-shelf, 96-well plate assay that standardizes incipient forebrain and spinal cord organoid morphogenesis as micropatterned, 3-D, singularly polarized neural rosette tissues (>9000 per plate). RosetteArrays are seeded from cryopreserved human pluripotent stem cells, cultured over 6-8 days, and immunostained images can be quantified using artificial intelligence-based software. We demonstrate the platform's suitability for screening developmental neurotoxicity and genetic and environmental factors known to cause neural tube defect risk. Given the presence of rosette morphogenesis perturbation in neural organoid models of NDDs and neurodegenerative disorders, the RosetteArray platform could enable quantitative high-throughput screening (qHTS) of human neurodevelopmental risk across regulatory and precision medicine applications.

INTRODUCTION

Human pluripotent stem cell (hPSC)-derived neural organoids are prominent *in vitro* models of human central nervous system (CNS) development. Their biological relevance complements, or in some respects exceed, traditional animal models[1–3]. Formed through spontaneous self-organization of differentiating hPSC aggregates, neural organoids can recapitulate extensive aspects of CNS tissue morphogenesis and obtain organotypic levels of neural cell phenotype diversity[4–8]. As such, they are promising tools for toxicological screening, disease modeling, and drug discovery[9]. However, in the absence of bioengineered controls, their emergent 3-D morphology, cytoarchitecture, and/or composition is variable, limiting inter- and intra-batch comparisons as well as scalability of post-hoc analyses[10,11]. This has impeded scalable implementation of neural organoid technology as a quantitative high-throughput screening

(qHTS) tool for detecting neurodevelopmental risk associated with genetic variants/mutations, i.e., genetic factors, and developmental neurotoxicity (DNT) associated with chemical or drug exposures, i.e., environmental factors. As a consequence, the multifactorial etiologies, i.e., combinations of genetic and environmental factors, of various human neurodevelopmental disorders (NDDs), e.g., neural tube defects (NTDs)[12,13], Autism Spectrum Disorder[14,15], and Schizophrenia[16], remains unclear. Overall, this impedes effective implementation of genetic screens for clinical risk assessment and discovery of precision medicine prophylactic and therapeutic approaches[17,18].

Neural rosettes comprised of polarized neuroepithelial cells (NECs), a.k.a. apical radial glial cells, model the inception of CNS morphogenesis and are the morphogenetic centers of neural organoids[19,20]. Each single rosette structure is mimetic of an embryonic neural tube slice, and depending on its rostrocaudal (R/C) and dorsoventral (D/V) patterning, constituent NECs can generate the comprehensive spectrum of region-specific brain or spinal neural phenotypes[21–23]. In standard neural organoid derivation protocols, rosettes emerge from non-planar, spheroidal cell aggregates in an uncontrolled manner, producing organoids with variable rosette number, size, and shape. This strays from *in vivo* development where the neural tube emerges from a neuroectodermal plate and forms a single lumen. This disparity causes a breakdown in reproducibility of organoid structure[23,24]. Recently, we and others have discovered that rosette emergence within nascent neural organoids can be controlled using biophysical constraints on initial cell aggregate morphology[21,25–27]. Specifically, we integrated micropatterned culture substrates with NEC derivation protocols[28,29] to enable enforcement of a prescribed 2-D cell monolayer morphology, which reproducibly instructs single rosette emergence upon morphing into a 3-D tissue[21]. Thus, this enables one to derive microarrays of nascent neural organoids with discrete R/C regionalization, reproducible single rosette structure, and in an adherent culture format that facilitates quantitative interrogation via microscopy, i.e., a RosetteArray. Importantly, micropatterned culture substrates can be scaled to higher throughput well plate formats, thereby enabling qHTS of early human CNS morphogenesis.

As an analogue to neural tube emergence, defects in neural rosette formation or perturbed behavior of its constituent cells can be predictive of factors that cause congenital NTDs[24,30,31], childhood-onset Autism Spectrum Disorders[14,20,32],Schizophrenia[16], and even adult-onset Huntington's disease[26] and frontotemporal dementia (FTD)/amyotrophic lateral sclerosis (ALS)[33].Thus, since neural rosette formation requires 'normal' hPSC viability, proliferation, neural differentiation, and NEC physiology, *in vitro* neural rosette formation could be a predictive tool for broadly assessing risk factors for a variety of NDDs as well as general DNT[34]. Regarding NTDs specifically, several groups have published the use of *in vitro* neural rosette formation assays to screen for environmental and genetic risk factors. However, these assays have significant limitations. First, rosette emergence was not standardized in space and time decreasing the assays' sensitivity[30,31,35]. Second, rosette emergence was only assessed in forebrain NECs or neural organoid cultures, whereas NTDs can occur at any point along the neural tubes' R/C axis[24,25,30,31]. In fact, NTDs of the lower spinal cord, i.e., myelomeningocele/spina bifida, are the predominant human clinical scenario[36]. Third, none of the prior neural rosette assays were conducted using direct seeding of cryopreserved cells, which is required to enable the type of scalable, 'off-the-shelf' qHTS necessary to effectively investigate DNT within chemical libraries as well as multifactorial NDD risk.

Here, we present development and validation of a hPSC-derived RosetteArray platform for scalable, off-the-shelf, qHTS of environmental and genetic factors, including clinically relevant multifactorial scenarios, known to cause neurodevelopmental risk. First, reproducible derivation

of forebrain (FB) and spinal cord (SC) RosetteArrays from direct seeding of cryopreserved hPSCs or neuromesodermal progenitors[22,28] (NMPs), respectively, was demonstrated. Second, the RosetteArray's capability to detect a risk associated with pharmaceuticals and agrochemicals known to cause NTDs was shown. These studies revealed differential responses between forebrain and spinal RosetteArrays to a well-known teratogen, supporting the importance of including both region-specific assays for more comprehensive coverage of CNS morphogenesis. Third, the RosetteArray platform was evaluated for general DNT assessment by screening a small library of pharmaceuticals and agrochemicals. This included exhibiting the ability to integrate human metabolism into the assay via compound pre-digestion with S9-pooled liver fraction. Fourth, scale-up of the RosetteArray to a 96-well plate format is demonstrated with maintenance of reproducible and efficient single rosette emergence. Fifth, since disruption of folate metabolism is the best known NTD-risk factor[37,38], RosetteArray detection of folate metabolic pathway antagonism, e.g., by Methotrexate and Dolutegravir, along with rescue by active folate supplementation was demonstrated. Lastly, gene-edited lines with mutations that perturb folate metabolic and planar cell polarity pathways[12,37] were created. Then, the RosetteArray platform's ability to detect genetic and multifactorial causes for NTD risk in a pathway specific and region-specific manner was observed. Collectively, these results support the RosetteArray platform's utility for qHTS of chemical DNT and factors that cause increased NTD risk. More broadly, they indicate that RosetteArrays could enable efficient investigation of multifactorial NDD etiology as well as screening to discover precision medicine prophylactic and therapeutic approaches.

RESULTS

Validation of an 'off-the-shelf" RosetteArray assay

Previously, we demonstrated that seeding WA09 hESCs[29] or cervical spinal NMP progeny[22,28] from culture onto micropatterned substrates could be used to generate FB and cervical SC RosetteArrays[21]. However, for scalable applications, an off-the-shelf protocol that uses direct seeding of cryopreserved cells is required to avoid errors caused by either genetic drift during long-term cell culture[39] and/or differences in hPSC culturing or NMP derivation between experiments. Thus, we cryopreserved banks of WA09 hESCs and cervical spinal NMP progeny, and tested whether their direct seeding onto micropatterned substrates could also generate FB and SC RosetteArrays in a 12-well format (**Figure 1A, B**). After 24-hrs post seeding in E8 media with 10 µm Rock inhibitor (R), prospective FB and SC RosetteArrays were cultured for an additional 5 days in E6 media without[29] or with retinoic acid (RA)[22,28], respectively, to permit differentiation into Pax6$^+$/N-cadherin$^+$ NECs with subsequent rosette emergence (**Figure 1C**). As previously optimized[21], FB and SC RosetteArrays were derived using micropatterned culture substrates presenting an array of 250 µm and 150 µm diameter circles, respectively, to preferentially induce single rosette emergence with regionally distinct tissue morphologies (**Figure 1D**). Post fixation and immunostaining, confocal Z-stacks of arrayed rosette tissues were collected and assessed for the number of DAPI$^+$ cells and the percentage of Pax6$^+$ NECs in the stack's middle slice using CellProfiler as previously described[21]. The percentage of rosette tissues displaying a single polarized structure was quantified manually. Retrospective analysis of FB RosetteArray data was used to determine that quantification of ~40-50 tissues per array is sufficient to estimate accurate and precise results for the entire array (**Figure S1A-C**). Using this threshold, it was determined that FB and SC RosetteArrays derived using direct seeding of cryopreserved cells yielded single neural rosette efficiencies of 68.35 ± 15.35% and 63.89 ± 14.62%, respectively (**Figure 1E**). Both values are lower than the 80-85% and 73.5% efficiencies observed previously for FB and SC RosetteArrays, respectively[21].

While concerned about the decrease in single rosette efficiency, we continued exploring the platform's utility for chemical screening by assessing its performance in media supplemented with dimethyl sulfoxide (DMSO), a common chemical library solvent. DMSO dose response experiments using FB and cervical SC RosetteArrays were conducted to investigate the solvent's effect on cell viability/proliferation (Cells/Tissue), neural induction[40] (%Pax6$^+$), and single rosette emergence (%Single Rosettes) (**Figure S2**). Both FB and SC RosetteArrays only showed cytotoxicity and inhibition of neural induction effects at DMSO levels exceeding 1.0% v/v. However, rosette emergence was inhibited at >0.1% DMSO v/v, representing its upper limit for use in RosetteArray assays. Interestingly, 0.1% DMSO media supplementation corresponded with a significant increase in FB RosetteArray single rosette emergence (91.69 ± 8.94%) but not in SC RosetteArrays (51.45 ± 6.00%) (**Figure 1E**). We attribute this region-specific effect to DMSO's known capacity for reversibly arresting hPSCs, but not NMPs, in the early G1 cell cycle phase thereby facilitating differentiation[41,42]. The SC RosetteArray's persistently lower single rosette emergence efficiency remained a concern, but collectively these results support the feasibility of deriving RosetteArrays by direct seeding of cryopreserved hPSCs and NMPs. Moreover, as demonstrated in other publications describing micropatterned morphogenesis of NEC-containing tissues[24–26], the hPSCs are seeded as a monolayer, and coincident with neural induction (Pax6$^+$/N-cadherin$^+$), morph into 3-D hemispherical forebrain tissues with a N-cadherin$^+$ polarized rosette structure by Day 5/6 of E6 media culture (**Figure 1F, G**).

FB RosetteArrays detect risk of NTD-associated teratogens.

NEC rosette emergence is an *in vitro* morphogenic analogue to *in vivo* neurulation. As such, we investigated whether FB RosetteArrays could detect the toxicity of compounds associated with clinically or epidemiologically based NTD risk (**Figure 2**). Glycolic acid (GA) was used as a negative control[43], and benomyl (BNM), valproic acid (VPA), methotrexate (MTX), and novobiocin (NVB) were used as positive controls. BNM has been epidemiologically correlated with NTDs and reported to antagonize the planar cell polarity (PCP) pathway, which is critical for neurulation[44,45]. VPA is an antiepileptic drug and well-known teratogen associated with NTD risk[46,47]. MTX is a chemotherapeutic and potent antagonist of the folate metabolic pathway, which is the best known NTD risk pathway[48,49]. Lastly, NVB is an antibiotic and potential chemotherapeutic that decreases the presence of extracellular matrix (ECM) protein fibronectin through inhibition of HSP-90[50]. Fibronectin plays a critical ECM role in early development and neurulation, and its NVB-mediated reduction at the neural/surface ectoderm interface was recently demonstrated to inhibit *in vitro* neural tube morphogenesis[25].

NTD-risk associated chemical exposures were initiated on the first day of FB RosetteArray neural induction (Day 0) and maintained for the assay's remaining 5 days (**Figure 1C**). Juxtaposition of dose-response curves for the RosetteArray's three primary metrics showed distinct profiles for each NTD risk compound. As expected[43], GA did not inhibit cell any RosetteArray metrics at the levels tested (**Figure 2A-D**). However, BNM exhibited cytotoxic (Cells/Tissue) effects along with inhibition of neural induction (%Pax6) and rosette emergence (Rosettes) at >1 µM (**Figures 2E-H and S3C, G)**. Similarly, VPA and MTX exhibited cytotoxicity at the highest tested concentrations (**Figure 2I, M**), but at non-cytotoxic concentrations, they also displayed inhibition of single rosette emergence (**Figures 2I-L, M-P and S3D, E, H, I**). For example, MTX's rosette emergence IC_{50} was ~25-fold and ~108-fold less than those noted for cytotoxicity and inhibition of Pax6 neural induction, respectively (**Figures 2P and S3I**). MTX's accentuated effect on rosette emergence is indicative of its targeted inhibition of the NTD-associated folate metabolic pathway[51]. Similarly, novobiocin also inhibited rosette emergence at concentrations showing no effects on cell viability/proliferation or neural induction metrics (**Figures 2Q-T and S3F, J)**. Interestingly, the FB RosetteArray detected novobiocin's NTD risk

despite not having non-neural ectodermal cells, i.e., the purported source of fibronectin matrix production in other *in vitro* neural tube models[25]. Overall, the sensitivity of the neural rosette morphogenic metric highlights the RosetteArray's ability to detect perturbations to pathways known to orchestrate *in vivo* neurulation and whose disruption causes NTD risk.

RosetteArray shows regional differences in VPA's NTD risk.
FB RosetteArray assays detect the NTD risk associated with VPA exposure showing complete inhibition of rosette emergence at ≥0.5 mM concentrations (**Figure 2I-L**). However clinically, VPA exposures are observed to predominantly cause NTDs in the spinal cord[52,53]. Thus, the effect of VPA exposure on cervical SC RosetteArrays was evaluated for comparison (**Figure 3A**). In contrast to FB RosetteArrays, VPA did not significantly inhibit cervical SC RosetteArray cell viability/proliferation, neural induction, or rosette emergence up to 0.5 mM (**Figure 3C-E**). Yet, the N-cadherin^{+} polarized ring area, i.e., 'Rosette Area', in cervical SC rosettes increased in a dose-responsive manner, which was a phenomenon not observed in VPA-exposed FB rosettes (**Figure 3B, F**). This indicates a region-specific response to VPA exposure captured by the RosetteArray platform, aligning with clinical data[52,53] and mouse embryo studies, in which VPA exposure biomechanically disrupts closure of the posterior neural tube[47]. Concordantly, we previously showed that biomechanical differences between FB and SC rosette tissues were responsible for needing different micropattern dimensions (i.e., 250 vs. 150 μm, respectively) to induce optimal singlular rosette emergence[21]. The ability to interrogate hPSC-derived neural rosette morphogenesis across the neuraxis is unique to the RosetteArray platform and may enables discrimination between adverse effects in rostral and caudal NTD mechanisms.

DNT screening using RosetteArrays with human metabolism integration.
To evaluate the use of RosetteArrays for general DNT assessment, FB RosetteArrays (12-well format) were used to screen a library of 29 pharmaceutical and agrochemical compounds (**Figure 1A and 4**). The library contained 6 negative and 23 positive controls, i.e., 'Reference Classification', as defined by anecdotal model organism toxicology data and literature review (**Figure S4**). Due to the 12-well plate format's limited scalability, each compound was assayed at a single 10 μM concentration in biological triplicate (**Figures S5,6,8**). This means that the sample size for the '%Single Rosette' metric is 3, i.e., each sample is the average of n=50 tissues analyzed per array/well, but the sample size for the 'Cells/Tissue', '%Pax6', and 'Rosette Area' metrics is up to 150. Due to the statistical power of having up to n=150, 'hits' for these metrics required a statistically significance difference that was >25% decrease from control. If only a statistically significance decrease was observed, then it was considered a 'Warning'. Additionally, for all compounds, the RosetteArray's three primary metrics were assessed first, and if no 'hit' was observed, then rosette area was also analyzed for further confirmation of non-toxic effects. Glycolic acid is the only exception to this rule given its well-known negative control status[43]. Lastly, to determine whether simulated human metabolism could be integrated into the RosetteArray platform, its tolerance for the presence of S9 pooled liver fraction was tested (**Figure S7**). Based on the dose-response, S9 is tolerated up to ~0.002 mg/mL concentrations in the assay media solution. Seven pesticides were screened both with and without S9 pre-digestion for DNT.

In the absence of simulated human metabolism, i.e., without S9 pre-digestion, 5 of 6 negative control compounds tested as true negatives (**Figure 4**, TN). Desmedipham, an herbicide, was detected as 'hit' due to a statistically significant decrease in rosette area, but it is not generally considered to have DNT effects[54]. Also, thalidomide is a well-known teratogen; however, it was referenced as a DNT negative because its teratogenic effects on limb formation are due to inhibiting angiogenesis[55]. Our screen indicated it as a 'warning' due to inhibition of cell

viability/proliferation. Of the positive controls, 22 out of 23 produced a hit with differential profiles indicating nuanced modes of action for each observed DNT. Cyproconazole is the only referenced positive control that did not produce a hit in the absence of simulated metabolism. Of note, Butyl benzyl phthalate is a plasticizer with known reproductive toxicity[56] and DNT in rodents[57], but there is limited human data regarding its DNT affect. In our screen, it only significantly perturbed rosette area potentially indicating a subtle effect. Also, Chlorpyrifos was a clear hit in our screen, supporting recent efforts to bans its use as a pesticide[58,59].

Seven pesticides were tested in the presence of simulated human metabolism. Desmedipham's previous toxicity disappeared with S9-predigestion prior to screening. Alternatively, Cyproconazole and Propyzamide became toxic upon being metabolized (**Figure 4**). This correlates with Cyproconazole's known disruption of Zebrafish development, including spinal malformations and locomotor defects[60,61]. Also, while Propyzamide has no known DNT effects, it is a known neurotoxicant in adult rats, alters gene expression associated with human developmental processes, and increases CYP450 enzymes upon human liver cell exposure[62]. Moreover, it disrupts tubulin-mediated microtubule assembly in plant cells[63], a process observed in hPSC-derived rosette morphogenesis[20]. Thus, while a Propyzamide-induced DNT was not observed without human metabolism in the RosetteArray or in other non-human model organism studies[61,64], it shows clear DNT in the FB RosetteArray after being metabolized, placing doubt on its 'Negative' reference classification (**Figure 4**). Across both metabolized and non-metabolized screens, the FB RosetteArray provided perfect specificity and near-perfect sensitivity DNT results, with the caveat of the studies small sample size and single-concentration evaluation. This demonstrates the platform's ability to integrate simulated human metabolism and potential for human DNT risk assessment.

Scale up to 96-well plate FB and SC RosetteArray assays.
While effective, the 12-well plate RosetteArray format is insufficient for qHTS applications due to limited throughput and the amount of test compound required. For scale up to a 96-well plate format, Willow® glass sheets were micropatterned and attached to bottomless 96-well plates using a double-sided adhesive as previously described[65] (**Figure 5A**). FB RosetteArray scale up experiments demonstrated that the 12-well plate protocol did not directly translate to the 96-well format (**Figure 5B-E**). In both E6 and 0.1%DMSO supplemented media conditions, Day 7 vs. Day 5 of culture was required to reach acceptable single rosette emergence efficiencies (i.e., 76.06 ± 14.94% and 86.27 ± 9.06%, respectively). Using Day 7 as the termination timepoint, the optimized 8-day FB RosetteArray protocol was reproducible across full 96-well plate screens. When conducted in biological quadruplicate, with 0.1%DMSO supplemented media, and using only the interior 60-wells, plate-wide averages for single rosette emergence were 91.83 ± 5.80%, 95.46 ± 5.81%, 86.67 ± 6.84%, and 91.46 ± 5.81% (**Figure S9A**). Additionally, the FB RosetteArray's Z-factor value is 0.532 across seventeen independent DNT screens using 1μM MTX and E6/0.1%DMSO as our positive and negative control conditions, respectively (**Figure S9B**).

For cervical SC RosetteArrays, direct protocol translation yielded even worse single rosette emergence results (**Figure 5F-I**). For 0.1% DMSO media conditions, the 96-well plate cervical SC RosetteArray's showed its best efficiencies at Day 5/7 of culture, but still much lower than the FB RosetteArray efficiency, especially in 0.1% DMSO supplemented media (**Figure 5D**). To improve the SC assay, its R/C regionalization and micropattern dimension were revisited in the 12-well format. Both cryopreserved cervical and lumbar-patterned NMPs[22] were seeded onto micropatterns of 100, 125, and 150 μm diameter circles and assessed for single rosette emergence at Day 5 of culture (**Figure S10A**). While single rosette emergence within cervical tissues did not vary significantly across the micropattern dimensions, lumbar-patterned rosettes

displayed increased (93.80 ± 4.10%) single rosette emergence on 100 μm diameter micropatterns (**Figure S10B-I**). When the lumbar SC RosetteArray protocol was directly translated to the 96-well plate format, similar single rosette emergence efficiencies were observed in 0.1% DMSO supplemented media (**Figure 5J-M**).

With successful scale-up to 96-well plate formats, RosetteArray analysis became a challenge. If automated confocal microscopy is used to acquire just 40 micropatterned tissues/well, then single rosette emergence within 3840 Z-stack images per plate could need to be analyzed manually (**Figure 5A**). Therefore, we utilized commercially available RosetteDetect™ software based on convolutional neural networks[66] to automate rosette detection and segmentation within such images. The artificial intelligence (AI) model was trained on 588 images and tested on a separate 5594 image set from DNT dose-response studies. Model validation studies on 'yes/no' identification of single rosette emergence yielded accuracy, precision, recall/sensitivity, specificity, and F1 values of >90% (**Figure S9C, D**). Also, the model's ability to segment the single rosette's polarized N-cadherin ring structure was tested across 128 images producing a Dice Coefficient of 88.64 ± 6.50%, indicating good agreement of the rosette's estimated area with manually curated ground truth data (**Figures 5A and S9E**). As a final demonstration of utility, RosetteDetect's performance in quantifying single rosette emergence across 3 DNT RosetteArray assays, i.e., Aspirin, Permethrin, and Rotenone, was compared to manual analysis. Dose-response curves generated using either manual or RosetteDetect analyses were statistically equivalent (**Figure 5N-P and S9F**). With inclusion of CellProfiler™ coding to quantify $DAPI^+$ and $Pax6^+$ cells/image slice, these results collectively demonstrate feasible scaling of RosetteArray assays and analysis for qHTS applications.

RosetteArrays detect chemical NTD risks specific to folate metabolic pathway inhibition. Of NTD risk pathways surveyed in Figure 2, disruption of folic acid metabolism is the best known NTD risk factor[48]. Therefore, the RosetteArray platform's ability to detect folate metabolic pathway specific NTD risk was interrogated further. First, we assessed the ability to rescue MTX inhibition of rosette emergence by supplementing with the metabolized form of folic acid, 5-methyltetrahydrafolic acid (5-MTHFA)[67]. 12-well FB RosetteArrays were used to conduct a MTX dose-response in the absence and presence of 20 μM 5-MTHFA (**Figure 6A-F and S11A, B**). In all metrics, the presence of 20 μM 5-MTHFA significantly shifted the dose-response curve to the right increasing IC_{50} values by greater >10-fold. This demonstrates folate metabolic pathway-specific rescue of MTX's inhibitory effects.

Second, the 12-well FB RosetteAssay was used to detect the NTD risk posed by Dolutegravir, an HIV antiretroviral therapy. When taken periconceptionally, Dolutegravir has been shown to increase clinical NTD occurrence[68,69], presumably by antagonistically binding the folate receptor-1[67]. Moreover, its NTD risk effects can be negated by sufficient folate dietary supplementation[67,70]. In our FB RosetteArray dose-response, Dolutegravir inhibits all metrics similarly with a single rosette emergence IC_{50} of 3.19μM (2.15-4.17μM, 95% CI), which is well within its therapeutic serum level of 3-10 μM[67] (**Figure S11C-G**). This is indicative of its presumed inhibition of folate receptor-1, which would inhibit vital folate metabolism required for basic cell physiology. Additionally, analogous to MTX, conducting the FB RosetteArray at 7.5 μM DTG with increasing 5-MTHFA concentrations showed a significant rescue in single rosette emergence and rosette area with non-significant but increasing trends in cell viability/proliferation and neural induction metrics (**Figure 6G-K**). Collectively, these results demonstrate that the FB RosetteArray can detect folate metabolic pathway-specific NTD risk associated with both MTX's inhibition of the pathway's dihydrofolate reductase enzyme and DTG's inhibition of folate receptor-1 binding [67].

Third, due to previous regional differences in RosetteArray responses to VPA (**Figure 3**), FB and lumbar SC RosetteArray detection of MTX's NTD risk was compared using the 96-well plate format (**Figure 6L-O**). Relative to the 12-well assay, the 96-well FB RosetteArray showed increased sensitivity to MTX's inhibitory effects with a >5-fold decrease in the single rosette emergence IC_{50} value, i.e., 0.069 μM (0.062-0.076 μM, 95% CI) vs. 1.4 μM (0.61-3.83 μM, 95% CI) vs. 0.351 μM (0.3-2.42 μM, 95% CI) (**Figure 6O, 2O, 6E, respectively**). Also, maximal inhibition of single rosette emergence was observed at ~1 μM vs. >100 μM in the 96- vs. 12-well FB RosetteArray formats (**Figures 6O, 2O**). When evaluating the 96-well plate format's regional differences, the lumbar SC RosetteArray had a statically equivalent $IC_{50,}$ i.e., 0.61 μM (0.035-0.10 μM, 95% CI), to the FB RosetteArray. Yet, its Lowest Observed Adverse Effect Level (LOAEL) was 500-fold lower than the FB RosetteArray, i.e., 0.1 nM (SC) vs 0.5 μM (FB) (**Figure 6O**). Moreover, above the IC_{50}, MTX inhibited single rosette emergence in SC and FB RosetteArrays similarly, but below the IC_{50}, SC tissues appeared more prone to form 2+ versus no rosettes per tissue (**Figures S12A-C**). Again, this highlights regional differences between rosette emergence mechanisms in FB vs. SC RosetteArrays mirroring presumed differences between regional NTD mechanisms *in vivo*[71].

RosetteArrays detect genetic and multifactorial NTD risks.
In addition to chemical exposures risks, genetic variants of folate metabolic and planar cell polarity (PCP) pathway machinery are also known to increase NTD risk[12]. To evaluate the RosetteArray platform's ability to detect such genetic risk factors, the WA09 hESC line was gene edited to generate clones with clinical $MTHFR^{C677T}$(p.A222V)[72] and $SCRIB^{C3128T}$ (p.P1043L)[73] variants. In the folate metabolic pathway, Methyltetrahydrofolate Reductase (MTHFR) generates 5-methyltetrahydrofolate, which is the metabolized folate form found in blood plasma[72]. The c.C677T mutation decreases the enzyme's activity by ~35% in heterozygotes and ~70% in homozygotes[74]. Sequencing revealed that the WA09 hESC line was heterozygous for the c.C677T mutation. Therefore, $MTHFR^{C677T(-/-)}$ homozygote clones #4 and #9 were generated using gene editing (**Figure S13A, B**). In the PCP pathway, the Scribble protein (SCRIB) acts to scaffold protein-complexes at the plasma membrane during epithelial cell apical-basal polarization[75]. Its N-terminal Leucine-Rich-Region (LRR) enables membrane localization, while its four PDZ domains, with the c.C3128T/p.P1043L mutation in its third PDZ domain, are reported to also effect membrane localization and PCP protein interactions[73,75] (**Figure S13C**). Gene editing of the WA09 parent line yielded a heterozygous ($SCRIB^{P1043L(+/-)}$, #78), a homozygous ($SCRIB^{P1043L(-/-)}$,#52), and a knockout ($SCRIB^{KO}$, #17) clone. The knockout was caused by a downstream deletion yielding a nonsense frameshift (**Figure S13D-G**). All clones could generate rosette containing cultures in standard 6-well forebrain NEC derivation experiments[29] (**Figure S13H-J**). Also, the parent and isogenic mutant lines had normal karyotypes with no mycoplasma detection (**Figure S14**).

To begin assessing the RosetteArray's sensitivity to NTD risk caused by the $MTHFR^{C677T(-/-)}$ variant, the $MTHFR^{C677T(+/-)}$ WA09 parent line and homozygous clones #4 and #9 were screened using 12-well FB RosetteArrays. The media used in the assay contains 9 μM folic acid. Therefore, this initial screen was run using control, 1 μM MTX, and 1 μM MTX plus 20 μM 5-MTHFA media conditions (**Figure S15A, B**). Of note, this experiment simulates a multifactorial NTD risk scenario, where the combination of the $MTHFR^{C677T}$ genetic variant and a MTX exposure are being modeled. No difference between lines in any metric is observed under

control FB RosetteArray conditions (**Figure S15C-E**). However, upon challenging with 1 μM MTX, all lines showed a statistically significant decrease in cell viability/proliferation and single rosette emergence metrics. Yet, both *MTHFR*$^{C677T(-/-)}$ clones demonstrated significantly increased MTX sensitivity in single rosette emergence, i.e., 13.62 ± 11.27% (Clone #4) and 23.47 ± 6.81%(Clone #9), compared to the *MTHFR*$^{C677T(+/-)}$ parent line, i.e., 51.50 ± 1.06%. This effect is folate metabolic pathway specific since 20 μM 5-MTHFA supplementation, in the presence of 1 μM MTX, rescued the risk phenotype in all lines.

To further clarify differences in folate metabolic pathway sensitivities, a full MTX dose-response in a 96-well FB RosetteArray was conducted comparing the *MTHFR*$^{C677T(+/-)}$ parent line, *MTHFR*$^{C677T(-/-)}$ clone #9, and the *MTHFR*$^{C677T(+/-)}$/ SCRIB$^{P1043L(-/-)}$ clone (**Figures 7A, B and 15F-I**). Each lines' dose-response yielded statistically different curves with the *MTHFR*$^{C677T(-/-)}$ clone #9's IC_{50} of 0.0305 μM (0.0200-0.0464 μM 95% CI) being lower than the *MTHFR*$^{C677T(+/-)}$/ SCRIB$^{P1043L(-/-)}$ clone's and *MTHFR*$^{C677T(+/-)}$ parent line's IC_{50}s of 0.0411 μM (0.0256-0.0656 μM 95% CI) and 0.0477 μM (0.0327-0.0686 μM 95% CI), respectively. For increased accuracy, a second MTX dose-response between the *MTHFR*$^{C677T(-/-)}$ clone #9 and its *MTHFR*$^{C677T(+/-)}$ parent line was conducted with additional dosages around the previously observed IC_{50} values and in biological duplicate (**Figure 7C and S15J-M**). Again, each lines' dose-response yielded statistically different curves but now without overlapping IC_{50} values, i.e., Clone #9- 0.0497 μM (0.0452-0.0544 μM 95% CI) vs. WA09 parent- 0.0697 μM (0.0629-0.0768 μM 95% CI). Additionally, a 5-MTHFA rescue dose-response in the presence of 1 μM MTX showed that *MTHFR*$^{C677T(-/-)}$ clone #9 required more folate supplementation, i.e., EC_{50} of 7.90 μM (5.38 - 11.20 μM 95% CI), than the *MTHFR*$^{C677T(+/-)}$ parent line, i.e., EC_{50} of 3.70 μM (2.57 -5.20 μM 95% CI) to rescue its risk phenotype (**Figure 7D-F and S15N-P**).Thus, the *MTHFR*$^{C677T(-/-)}$ lines' increased sensitivity to folate metabolic pathway perturbation is due to its additional c.C677T mutation compared to the *MTHFR*$^{C677T(+/-)}$ parent line. Moreover, this highlights the RosetteArray platform's ability to quantify a genetic NTD risk factor in a multifactorial scenario.

To model PCP pathway-induced NTD risk, SCRIB$^{P1043L(+/-)}$, SCRIB$^{P1043L(-/-)}$, and SCRIB^{KO} lines were generated and cryopreserved as both hESC and cervical spinal NMP banks along with the WA09 parent line (**Figure S16A**). In 12-well FB RosetteArrays, no difference was observed between the 3 mutant lines despite immunostaining showing FB rosette formation in the absence of SCRIB protein for the knockout mutant (**Figures 7G-K and S16B**). Yet, in the 12-well cervical SC RosetteArray, there was complete abrogation of rosette emergence accompanied by a significant decrease in cell viability/proliferation and neural induction in the SCRIB^{KO} line compared to the SCRIB$^{P1043L(+/-)}$ and SCRIB$^{P1043L(-/-)}$ lines (**Figure 7G,H, L-M**). This regional NTD risk phenomenon in the SCRIB^{KO} line comports with the *SCRIB*^{Crc} mouse[75] and human[76] presentation of craniorachischisis (CRN), which is a failure of neural tube closure across the neuraxis except for the rostral forebrain[77]. Also, despite SCRIB's p.P1043L mutation in its third PDZ domain, immunostaining showed apical co-localization of SCRIB and F-Actin (phalloidin) in both FB and cervical SC rosettes (**Figure S16B**). However, SCRIB^{KO} rosettes showed F-Actin apical polarization in FB Rosettes despite minimal-to-no SCRIB immunostaining, and no F-actin polarization in cervical SC rosettes. In mice, others have observed that SCRIB mutations, which lower expression (*SCRIB*$^{rumz/rumz}$) causing CRN, also cause decreased apical immunostaining of F-actin and other tight junction proteins in defect presenting regions[75].

This striking R/C regional difference led us to investigate expression of SCRIB in FB and cervical SC rosette tissues. In humans, SCRIB has two isoforms (A and B) with SCRIB A containing a c-terminal AbLIM domain that links the protein to F-actin through binding β spectrins[78] (**Figure S13C**). Using qPCR for all SCRIB and its isoforms across the WA09 parent and each SCRIB mutant line, we observed a decreasing trend in expression of all SCRIB and isoform B as cells transitioned from hESC to FB NEC and SC NMP and NEC states (**Figure S16C**). However, the SCRIB A isoform displayed a unique increase in FB NECs in all lines except for the $SCRIB^{KO}$, confirming its knockout status. Overall, this data suggests a FB-SC regional difference in the importance of SCRIB for NEC apical-basal polarization that motivates further investigation. Additionally, it again highlights potential R/C regional differences in NTD mechanisms and motivates NTD risk assessment the across the neuraxis as enabled by the RosetteArray platform.

DISCUSSION

The RosetteArray platform standardizes morphogenesis of hPSCs into incipient forebrain and spinal neural organoids, a.k.a. single rosette tissues[21], thereby providing a predictable analogue of human neural tube emergence for screening applications. To our knowledge, it's the first hPSC-derived rosette/neural tube morphogenesis assay that can be generated using direct seeding of cryopreserved cells, thereby enabling an off-the-shelf assay[24,25,27,30] (**Figure 1**). Our results demonstrate its promise as a human neurodevelopmental risk assessment tool for general DNT screening and for modeling NTD risk factors. Evaluation with 31 different chemicals with known NTD risk/DNT profiles demonstrated that the RosetteArray yields preliminary DNT specificity and sensitivity values of 1.0 and 0.83, respectively (**Figure 2, 4, S11C-G**). The only negative control missed was Propyzamide, of which its 'negative' assignment in a human metabolized scenario is questionable[62,63]. Also, our experiments showed that the platform, using both FB and SC RosetteArrays, can reliably detect environmental/chemical, genetic, and multifactorial NTD risk factors (**Figures 5,6**). Interestingly, some NTD risk factors demonstrated region-specific perturbations of rosette morphogenesis (**Figures 3,7G-N**), indicating the importance of encompassing diverse neuraxial regions in DNT assays. Lastly, with scaling to a 96-well plate format plus AI-based image analysis (**Figure 5**), the RosetteArray enables off-the-shelf, qHTS of broad human neurodevelopmental risk as demonstrated here and elsewhere for Autism Spectrum Disorder[20].

Nearly two decades ago, US regulatory agencies stated the need for developing New Alternative/Approach Methodologies (NAMs) to better recapitulate human biology for risk assessment purposes and to reduce the use of animal testing[79,80]. Specific to DNT, the Organization for Economic Cooperation and Development recently released a DNT in-vitro testing battery guideline, which includes assays for neural progenitor cell proliferation, apoptosis, and cell migration but lacked a scalable neural rosette formation assay[81]. The RosetteArray platform provides this assay by enabling spatial and temporal prediction of rosette morphogenesis, which encompasses hPSC viability, proliferation, neural differentiation, and NEC viability, proliferation, and rosette morphogenesis[34]. Additionally, we and others have used rosette morphogenesis to assess risk of other neurodevelopmental[16,20] and neurodegenerative[26,33] disorders. Thus, further exploration into the extent to inclusion of RosetteArray assay could streamline the DNT in-vitro testing battery is warranted. This would help achieve the regulatory goal of providing optimal human DNT risk assessment while

balancing industry's goal for efficient and cost-effective tools for safety assessment in discovery pipelines.

NTDs are well known to have environmental, polygenic, and multifactorial etiologies, which have historically been investigated using mouse models[12]. This approach has and continues to provide fundamental insights. Yet, it has inherent translational and experimental limitations. Translational limitations caused by differences between mice and humans include genomic sequence/architecture, number of neural tube closure points, and the fact that mouse models predominantly display cranial defects versus spina bifida defects being the majority of human clinical cases[71,82]. Experimentally, the limited number of mouse strains used to create NTD models impedes exploration of how population variation affects polygenic etiology[71]. Also, experimental possibilities are limited by the sheer number of mice required for regulatory DNT studies, i.e. n=20 per experimental group[83], or to demonstrate the rate of NTD occurrence. For example, Tukeman et al. required the use of 169 dams/1302 fetuses in order to observe 7 NTD cases and demonstrate the folate-responsive NTD risk associated with periconceptional DTG administration[70].

The RosetteArray platform helps to address these limitations by providing a hPSC-derived analog of FB and SC neural tube emergence. It displays regional differences in morphogenesis[21] (**Figures 1D, 5D, H, S10**) and NTD risk responses (**Figure 3, 6O, 7G-N, S12**) that may be indicative of known differences in neural tube closure mechanisms[71]. Using FB RosetteArrays, DTG's folate-responsive NTD risk was detected at therapeutic serum levels (**Figure 6G-K, S11C-G**), further supporting clinical[69] and rodent studies[70]. Also, since the platform can be derived using iPSC lines[20], it could enable population variation studies to, for example, elucidate polygenic and multifactorial etiologies underlying *MTHFR*^{C677T} penetrance in NTD cases. Using just two FB RosetteArray 96-well plates (biological replicates), we observed an increased NTD risk (TC vs. TT IC_{50} ratio = 1.40) associated with *MTHFR*^{C677T} homo- vs. heterozygosity in the WA09 genetic background (**Figure 7C**). A finding recapitulated in meta-analysis of 19 different clinical studies with ~6438 participants that yielded a TC vs. TT odds ratio of 1.427 (1.247-1.634, 95% CI)[84]. While IC_{50} ratios and odds ratios are not comparable, it does support further use of the RosetteArray for conducting NTD etiology studies to investigate population variance. Coupled with the platform's ability to enable *in vitro* observation of SCRIB^{KO}'s R/C region-specific NTD risk phenomena, which is clinically associated with CRN[75], RosetteArray technology could have a transformative impact on investigating human NTD etiology, despite lacking non-neural components that surround the emergent neural tube *in vivo* (**Figure 2Q-T, S3F, J**)[25,85]. Moreover, the RosetteArray platforms could be scalably applied to elucidating the etiology of other NDDs and for qHTS of precision medicine therapeutics to prevent or mitigate the severity of such disorders.

AUTHOR CONTRIBUTIONS

B.F.L, G.T.K., and R.S.A. took part in conception and design of all RosetteArray experiments and jointly interpreted all data. K.K. and R.W. conceived and designed all RosetteDetect experiments and jointly interpreted all related data. B.F.L. and G.T.K. performed all RosetteArray experimentation unless otherwise noted. N.J.K. performed all RosetteArray assays whose control data was included in Z-factor analysis. N.R.I. aided in derivation of WA09 and *SCRIB* mutant cell banks. B.F.L., G.T.K., N.J.F., J.E.M., and M.R.C. performed data acquisition and data analysis. N.R.Iz. and J.E.M. assisted with platform manufacturing, immunostaining, and imaging. J.F.R. and B.J.I. assisted with design and interpretation of DNT

and NTD experiments. B.F.L, G.T.K., and RSA drafted the manuscript for publication with comments from all authors.

ACKNOWLEDGEMNTS

We thank Ainhoa Letamendia for assistance with DNT library formulation and anecdotal data. We thank the University of Wisconsin-Madison's Human Pluripotent Stem Cell and Gene Editing Service for generating *MTHFR* and *SCRIB* mutant lines. They are supported, in part, by a NICHD U54HD090256 grant and UW2020 Grant awarded to Anita Bhattacharyya and Su-Chun Zhang by the UW-Madison and the Wisconsin Alumni Research Foundation. B.F.L, N.J.F., and R.S.A were supported by NICDH R21HD103111 grant awarded to the Ashton lab at UW-Madison. G.T.K., N.J.F., K.K., R.W., and R.S.A. were supported by NIEHS R42ES033912 grant awarded to Neurosetta LLC. B.F.L. was also supported by NIH MSTP T32GM14095. G.T.K. and R.S.A. were also supported by Draper TIF grant #AAH6969 and a WARF Accelerator grant #AAI6923 awarded by WARF. N.R.I. and R.S.A. were also supported by U.S. Environmental Protection Agency grant 83573701. R.S.A. was also supported by NIH UG3TR003150, NSF CAREER Award #1651645, and an Innovation in Regulatory Science Award #1014150 from the Burroughs Wellcome Fund. R.W. was also supported by NSF awards DMS-AWD00000326 and PHY2317138 and the Simons Foundation award MP-TMPS-00005320.

DECLARATION OF INTERESTS

G.T.K, R.W., and R.S.A are co-founders and co-owners of Neurosetta LLC, which focuses on commercializing RosetteArray™ technology for human neurodevelopmental risk assessment. N.J.F. and K.K. are employees at Neurosetta LLC.

STAR Methods

KEY RESOURCES TABLE

REAGENT or RESOURCE	SOURCE	IDENTIFIER
Antibodies		
SCRIB primary	Invitrogen	(Thermo Fisher Scientific Cat# PA5-54821, RRID:AB_2647030)
N-cadherin primary	BD Biosciences	(BD Biosciences Cat# 610920, RRID:AB_2077527)
Pax6 primary	BioLegend	(BioLegend Cat# 901301 (also 901302), RRID:AB_2565003)
β-tubulin primary	Biolegend	(Cat# 802001, RRID:AB_2564645
Brachyury primary	R&D	Cat# AF2085, RRID:AB_2200235
Sox2 primary	Millipore	Cat# MAB4423, RRID:AB_11213224
Donkey anti-Rabbit IgG 488	Invitrogen	(Thermo Fisher Scientific Cat# A-21206 (also A21206), RRID:AB_2535792)
Donkey anti-Mouse IgG 488	Invitrogen	(Thermo Fisher Scientific Cat# A-21202, RRID:AB_141607)
555 Donkey anti-Rabbit	Invitrogen	(Thermo Fisher Scientific Cat# A-31572 (also A31572), RRID:AB_162543)
Donkey anti-Mouse IgG 555	Invitrogen	(Thermo Fisher Scientific Cat# A-31570, RRID:AB_2536180)

horseradish peroxidase-conjugated goat anti-rabbit	Jackson ImmunoResearch Laboratories	(Jackson ImmunoResearch Labs Cat# 111-035-003, RRID:AB_2313567)
Chemicals, Peptides, and Recombinant Proteins		
ROCK Inhibitor (Y27632)	Tocris	Cat#: 1254
FGF8b	PeproTech	Cat#: 100-25
CHIR99021	Tocris	Cat#: 4423
GDF11	PeproTech	Catalog Number:120-11
Dorsomorphin	Tocris	Cat#: 3093/10
Retinoic Acid	Sigma-Aldrich	Cat#: R2625
Penicillin-Streptomycin	Invitrogen	Cat#: 15140122
TRIzol	Invitrogen	Cat#: 15596026
Triton X-100	Sigma-Aldrich	Cat#:A16046.AE
DAPI	Invitrogen	Cat#: D1306
Alexa Fluor 488 Phalloidin	Invitrogen	Cat#: A12379
ω-mercaptoundecyl bromoizobutyrate	ProChimia	Cat#: FT 015-m11-0.2
PEGMEMA	Sigma-Aldrich	Cat#: 447935
sodium ascorbate	Sigma-Aldrich	Cat#: 1613509
2,2’-Bipyridine	Sigma-Aldrich	Cat#: D216305
Copper (II) Bromide	Sigma-Aldrich	Cat#: 221775
human S9 liver fraction	Sigma-Aldrich	Cat#: S2442
CloneR	StemCell Technologies	Cat#: 05889
TrueCut Cas9 Protein V2	Thermo Fisher Scientific	Cat#: A36498
QuickExtract DNA Extraction Solution 1.0	Thermo-Fisher	Cat#: NC9904870
protease inhibitors	Thermo-Fisher	Cat#: 78429
Glycolic Acid	Sigma-Aldrich	Cat#: 124737
Benomyl	Sigma-Aldrich	Cat#: 45339
Valproic Acid Sodium Salt	Sigma-Aldrich	Cat#: P4543
Methotrexate	Sigma-Aldrich	Cat#: 1414003
Novobiocin	Sigma-Aldrich	Cat#: N6160
Dabigatran	Sigma-Aldrich	Cat#: SML2351
Acetaminophen	Sigma-Aldrich	Cat#: A7085
Acetochlor	Sigma-Aldrich	Cat#: 33379
Pymetrozine	Sigma-Aldrich	Cat#: 46119
Clodinafop	Sigma-Aldrich	Cat#: 31676
Fenoxycarb	Sigma-Aldrich	Cat#: 34343
Thalidomide	Sigma-Aldrich	Cat#: T151
Butyl benzyl pthalate	Sigma-Aldrich	Cat#: 36927
Heptadecafluorooctane-sulfonic acid	Sigma-Aldrich	Cat#: 77282

Methyl mercury	Sigma-Aldrich	Cat#: 442534
Verapamil	Sigma-Aldrich	Cat#: V4629
Carbamazepine	Sigma-Aldrich	Cat#: C4024
Propiconazole	Sigma-Aldrich	Cat#: 45642
Abamectin	Sigma-Aldrich	Cat#: 31732
Benzylcetyldimethyl Ammonium Chloride	Sigma-Aldrich	Cat#: B4136
Spirodiclofen	Sigma-Aldrich	Cat#: 33654
Thiram	Sigma-Aldrich	Cat#: 45689
Triadimefon	Sigma-Aldrich	Cat#: 45693
Epoxiconazole	Sigma-Aldrich	Cat#: 36848
Desmedipham	Sigma-Aldrich	Cat#: 45426
Fenhexamid	Sigma-Aldrich	Cat#: 31713
Cyproconazole	Sigma-Aldrich	Cat#: 46068
Chlorpyrifos	Sigma-Aldrich	Cat#: 45395
Propyzamide	Sigma-Aldrich	Cat#: 45645
Thiacloprid	Sigma-Aldrich	Cat#: 37905
Aspirin	Sigma-Aldrich	Cat#: A2093
Permethrin	Sigma-Aldrich	Cat#: 45614
Rotenone	Sigma-Aldrich	Cat#: 45656
5-methyltetrahydrofolic acid, disodium salt	Sigma-Aldrich	Cat#: M0132
Dolutegravir	Sigma-Aldrich	Cat#: 10313
Critical Commercial Assays		
RPS18 Taqman Gene Expression Assay	Thermo-Fisher	Cat#Hs01375212_g1
SuperScript IV First-Strand Synthesis System	Invitrogen	Cat#: 18091050
Neon™ Transfection System	Invitrogen	Cat#: MPK10096
Zymoclean Gel DNA Recovery Kit	Zymo Research	Cat#: D4007/D4008
DC Protein Assay	Bio-rad	Cat#: 5000111
Experimental Models: Cell Lines		
WA09 hESC line (parent of all edited lines)	WiCell	(RRID:CVCL_9773)
Oligonucleotides		
HoxA1 Taqman Gene Expression Assay	Thermo-Fisher	Cat#Hs00939046_m1
HoxA5 Taqman Gene Expression Assay	Thermo-Fisher	Cat#Hs00430330_m1
HoxC6 Taqman Gene Expression Assay	Thermo-Fisher	Cat#Hs00171690_m1
HoxC8 Taqman Gene		Cat#Hs00224073_m1

Expression Assay	Thermo-Fisher	
HoxC9 Taqman Gene Expression Assay	Thermo-Fisher	Cat#Hs00396786_m1
HoxD10 Taqman Gene Expression Assay	Thermo-Fisher	Cat#Hs00157974_m1
All SCRIB Taqman Gene Expression Assay	Thermo-Fisher	Cat#Hs00363005_m1
SCRIB Iso A Taqman Gene Expression Assay	Thermo-Fisher	Cat#Hs01034954_g1
SCRIB Iso B Taqman Gene Expression Assay	Thermo-Fisher	Cat#Hs01040361_g1
Software and Algorithms		
CellProfiler	Harvard	v4.2.6
GraphPadPrism	GraphPad Prism	v10.2.1
Nikon NIS-Elements (Acquisition)	Nikon	v5.42.01
Nikon NIS-Elements AR (Analysis)	Nikon	v5.02.00
RosetteDetect™	Neurosetta LLC	v0.1.0.0
Other		
CryoMed controlled rate freezer	Thermo Fisher Scientific	Cat#: TSCM17PA
Prolong Gold Antifade Reagent	Invitrogen	Cat#: P36930
Nikon A1R confocal microscope	Nikon	n/a
4–20% Mini-PROTEAN® TGX™ Precast Gel	Bio-rad	Cat#: 4561094

Lead Contact

Further information and requests for resources and reagents should be directed to and will be fulfilled by the Lead Contact, Randolph Ashton (rashton2@wisc.edu).

Materials Availability

- Edited hPSC cell lines available upon request to lead contact.

Data and Code Availability

- Any additional information required to reanalyze the data reported in this paper is available from the lead contact upon request.

Data

All data used for statistical analysis is included in the Supplemental Data excel file. All data reported in this paper will be shared by the lead contact upon request.

Code

- This paper does not report original code. RosetteDetect™ software is available at https://neurosetta.com/rosette-detect/ for use by the public.

Experimental Model and Subject Details

Cell Lines
WA09 (H9, XX) hESC were supplied by the WiCell Research Institute. WA09 hESCs and the gene edited derivates were maintained at 37°C in 5% CO_2 in E8 medium under feeder-free conditions on Matrigel (WiCell)-coated 6-well plates (Corning). For maintenance and expansion, the cells were subcultured in Versene every 5 days at a 1:12 ratio following ~85% confluency. For cell line authentication, each cell line (WA09 parent and 5 edited clones) was submitted to WiCell for karyotyping and mycoplasma testing and results returned validated (Figure S14).

Method Details

RosetteArray Culture Substrate Fabrication
Culture substrates for 12-well RosetteArray assays were generated in accordance with our previously published protocol[21]. In brief, Polydimethylsiloxane (PDMS) stamps featuring rectangular arrays of circular recessions with 250, 150, and 100 µm diameters were used to transfer and establish a self-assembled monolayer (SAM) of 2 mM ω-mercaptoundecyl bromoizobutyrate onto gold-coated No. 1 glass coverslips. Poly(ethylene) glycol methyl ether methacrylate (PEGMEMA) brushes were grafted from these SAMs using sodium ascorbate-initiated atom transfer radical polymerization (ATRP) under inert gas for 16 hours at room temperature. Trace copper ions and residual organic solvents were removed through subsequent washes with 70% ethanol. 96-well RosetteArray plates were obtained from Neurosetta LLC.

NMP Derivation
WA09 hESCs and gene-edited mutants were differentiated into NMPs as previously described[22,28] utilizing CHIR99021, FGF8b, GDF11, and dorsomorphin. Briefly, hESCs were seeded at a density of 1.5×10^5 cells/cm^2 in E8 medium with 10 µM ROCK inhibitor for 24 hours. The medium was replaced with E6 medium on day 0 and then changed to E6 supplemented with FGF8b (200 ng/ml) 24 hours later (day 1). On day 2, cells were subcultured at a 2:3 ratio by washing once with PBS, incubating in Accutase for ~2 minutes, and removing them from the surface with gentle pipetting. After centrifugation, cells were gently resuspended in NMP medium, i.e., E6 medium with FGF8b (200 ng/ml) and 3 µM CHIR99021, containing 10 µM Y27632 and seeded on Matrigel-coated plates. This initiates *HOX* colinear and combinatorial expression and is referred to as 'Hox0', with 0 representing the hours of CHIR exposure. NMP medium was replenished on day 4 (Hox48). On day 5 (Hox72), cervical spinal cells were collected for cryopreservation (see next section). Lumbar spinal cells used in the paper were taken directly from previously generated cryopreserved banks[22] but they can be derived by caudalizing past the Hox72 time point. On day 5, cells should be subcultured (2:3) as before using NMP media. On day 7-10, the media should be replenished daily but now supplemented with GDF11 (30 ng/ml) and 1 µM dorsomorphin to stimulate caudal NMP development. On day 9, the cultures should be subcultured at a 1:1 ratio. On day 11 (Hox216), lumbar cells can be collected for cryopreservation.

Cryopreservation and Thaw of hESCs and NMPs
Confluent monolayers of WA09 hESCs in 6-well plates were prepared for cryopreservation through enzymatic dissociation in Accutase (ThermoFisher) and resuspend at ~6,000,000 cells/mL in E8 medium with 10 µM ROCK inhibitor Y-27632 and 10% DMSO. WA09-derived NMPs were similarly dissociated in Accutase and resuspended in E6 medium at ~6,000,000 cells/mL with 10 µM ROCK inhibitor and 10% DMSO. Cryopreservation was performed in Cryovials (Wheaton, Ref#: W985922) at 1mL/vial using a Thermo Scientific CryoMed Controlled-Rate Freezer (7450) set to lower temperature at the following rates; -10°C/min to 4°C, -1°C/min to -60°C, and -10°C/min to -100°C. Cryopreserved vials of cells were placed in

liquid nitrogen dewars for extended storage. Cells were thawed at 37°C for 3-5 mins and resuspended in E8 medium with 10 µM ROCK inhibitor for hESC seeding or E6 medium with 10 µM ROCK inhibitor and 1 µM RA for NMP seeding.

Forebrain and Spinal Cord RosetteArray Derivation

FB RosetteArray derivation was initiated by thawing and seeding cryopreserved hESCs at ~200,000 cells/cm^2 onto Matrigel-coated micropatterned arrays with 250 µm diameter circular regions in E8 medium with 10 µM ROCK inhibitor Y-27632. After 1 day, they were cultured in E6 medium for 5-7 subsequent days using daily 50% media changes. SC RosetteArray derivation was initiated by thawing and seeding cryopreserved hNMPs[22] at ~150,000 cells/cm^2 onto Matrigel-coated micropatterned arrays with 100 or 150 µm diameter circular regions in E6 medium, 10 µM ROCK inhibitor Y-27632, and 1 µM Retinoic Acid. After 1 day, they were cultured in E6 medium with 1 µM RA for 5 subsequent days using daily 50% media changes. Neuroectoderm monolayers were generated analogously in Matrigel-coated 6 well plates, without the use of micropatterned substrates. All culture was performed in tissue culture polystyrene plates (Corning) in medium supplemented with Penicillin/Streptomycin (ThermoFisher). Standard derivation experiments required E6 medium supplementation with DMSO (Sigma-Aldrich) at 0.01% and 0.1% v/v.

RosetteArray DNT Testing

All DNT compound screening involved supplementation of the culture medium beginning 1 day after cell seeding and upon removal of ROCK inhibitor. Chemical compound stocks were prepared from dry stock, fresh for each experiment, and solubilized in DMSO or water. Dose response medium formulations were prepared through serial dilutions in E6 medium. Compound concentrations were doubled in formulations to account for 50% medium changes. Compounds solubilized in DMSO were normalized to control conditions containing DMSO supplementation matching the highest tested concentration of DMSO in the treatment groups. Enzymatic digestions of compounds for simulated metabolism experiments were performed with human S9 liver fraction. Compounds were digested at 1 mM concentrations with and without S9 liver fraction at 2 mg/mL for 1 hour at 37°C in 200 mM Tris buffer containing 40 mM NADPH. Digestions were terminated via aliquoting and freezing at -20°C. Dose response experiments with digested compounds were performed by daily thawing of fresh aliquots.

Immunocytochemistry

On the last day of culture, RosetteArrays were fixed in 4% paraformaldehyde (PFA) in PBS for ~15 minutes. Micropatterned tissues were permeabilized and blocked with 0.1% Triton-X and 5% Donkey serum in PBS (PBS-DT) for 1 hour at room temperature. Primary antibodies listed in the Key Resource Table were incubated on the substrates at 4°C overnight and at a 1:200 dilution in PBS-DT. This was followed by 3 x 20-minute washes with PBS-DT. Next, secondary antibodies listed in Key Resources Table were incubated on the substrates at 4°C overnight and at a 1:500 dilution in PBS-DT. This was followed by 2 x 20-minute washes with PBS-DT, and cell nuclei were stained with DAPI for 10 minutes in the last PBS wash.

Image Acquisition

A Nikon AR-1 Scanning Confocal Microscope with an HD upgrade, Nikon DUG with GaAsP detectors, and a JOBS module software upgrade was used to acquire all fluorescent images. The JOBS module enables semi-automated image acquisitions. In each well, a 10x image was used to randomly selected tissues from the array. High definition, resonance or Galvano scanning image acquisition was performed using a 10, 20, or 60X objective (Nikon) at 512x512 (resonance) or 4096 x 4096 (Galvano) pixels to create Z-stacks with 5-7 image planes at 1.5 µm Z-axis spacing.

Image Analysis
Image segmentation (CellProfiler, Harvard) was used to quantify the number of $DAPI^+$ and $Pax6^+$ cells per image plane for each rosette. To minimize double counting of cells between image planes, only the middle image plane in a Z-stack was used to generate a relative number of cells (# of $DAPI^+$ cells) and $\%Pax6^+$ (# of $Pax6^+$ cells / # of $DAPI^+$ cells) per tissue. Single rosette emergence was quantified through manual and RosetteDetect™ image analysis. For manual analysis, each tissue Z-stack was interrogated and scored as a binary single rosette structure ('1') or no or >1 rosette ('0'). Neural rosettes in micropatterned tissues were identified by the presence of a coherent, polarized, N-cadherin$^+$ or Phallodin$^+$ ring structure. Percent neural rosette emergence was calculated as # single rosette-presenting vs. analyze tissues (n=40-50) per array. In single rosette tissues, rosette morphological characteristics were measured by outlining the boundary of the N-cadherin ring.

Calculation of Z' Factor
The Z' Factor was calculated as: $Z' = 1- (3(\sigma_{postive} + \sigma_{negative})/|\mu_{positive} - \mu_{negative}|)$. Where $\sigma_{postive}$ and $\sigma_{negative}$ represent the positive (1.0 µM Methotrexate) and negative (E6/0.1% DMSO) controls' standard deviation, and $\mu_{positive}$ and $\mu_{negative}$ are their respective means.

Calculation of the LOAEL
In the MTX dose-response experiment, %single neural rosette averages for each dose were compared to the experimental condition's solvent control via a Student's T-test within Excel. The first dose that was significantly different from the solvent control at a level of $p<0.05$ was considered the lowest-observed-adverse-effect level (LOAEL).

Non-linear Regression of Dose-response Curves
GraphPad Prism was used to calculate parameters associated with the Logistic Regression Model, plot sigmoidal dose-response curves, and analyze the curves' fit for different parameters plus calculation of the 95% CIs and R^2 values.

CRISPR/Cas9 gene editing
The UW-Madison Human Stem Cell Editing Core was used to create *MTHFR* and *SCRIB* gene-edited lines. sgRNA sequence identification for each editing site was completed using the CRISPOR design tool[86]. The sgRNAs were ordered from Synthego as a 1.5 nmol synthetic sgRNA with 2'-O-methyl 3' phosphorothioate modification at the first and last 3 nucleotides following the recommended suggestion. hPSCs were cultured in TeSR-PLUS media (StemCell Technologies) on Matrigel until ~80% confluency following standard cell culture protocols. Twenty-four hours before electroporation, cells were treated with CloneR (StemCell Technologies) following manufacturer protocol. Prior to the electroporation, the required sgRNA constructs were reconstituted following manufacturer protocols to a concentration of 150 pmole/µL. 1 µL of reconstituted sgRNA was pooled with 4 µg Cas9 Nuclease protein (TrueCut Cas9 Protein V2, Thermo Fisher Scientific) and 5 µL of Neon Buffer R (Invitrogen) to promote Cas9-RNP complex formation. After 15 minutes, 1.0 µL of ssODN primer (reconstituted to 1 µg/µL concentration, designed with homology overhangs of at least 40 base pairs) was added to the Cas9-RNP mix. Cells were singularized and lifted with a 1:1 mixture of 0.5 mM EDTA: Accutase for 3-4 minutes, resuspended in 1 mL PBS, and pelleted. Approximately 400,000 cells were resuspended in 35 µL Buffer R and mixed with 8 µL of the pre-prepared Cas9-RNP complex with repair ssODN. Cells were electroporated with a 10 µL NEON electroporation format using 1200V, 30 msec, 1x pulse settings. Cells were pooled following four rounds of electroporation and plated in TeSR-PLUS media with CloneR supplement at manufacturer-recommended concentrations following a serial dilution to promote single-cell clonal growth.

Following expansion of 10-14 days, clones were identified and picked using standard techniques.

Genotyping

Bulk gDNA was collected from dissociated cells using QuickExtract DNA Extraction Solution 1.0 (Epicentre) to confirm editing efficiency prior to clonal selection. Single-cell clones were manually selected and mechanically disaggregated. Genomic DNA was isolated from a portion of these clones using QuickExtract DNA Extraction Solution 1.0. Genotyping primers were designed flanking the mutation site, allowing amplification of this region using Q5 polymerase-based PCR (NEB). PCR products were identified via agarose gel and purified using a Zymoclean Gel DNA Recovery Kit (Zymo Research). Clones were submitted to Quintara Biosciences for Sanger sequencing to identify clones with the proper genetic modification.

Off-target analysis

To identify whether the CRISPR-Cas9 system produced any non-specific genome editing, we analyzed suspected off-target sites for genome modification. Using the 5 highest-likelihood off-target sites for each sgRNA as predicted by the CRISPOR algorithms, we designed genotyping primers to amplify these regions via Q5-polymerase PCR. PCR products were identified via agarose gel, purified using a Zymoclean Gel DNA Recovery Kit, and submitted to Quintara Biosciences for Sanger sequencing.

Karyotyping

Live cells for all utilized cell lines and edited clones were submitted to WICell for karyotype analysis (Figure S14).

qPCR and gene expression analysis

Total RNA was isolated using a TRIzol reagent (Invitrogen), and complementary DNA (cDNA) was synthesized using the SuperScript IV First-Strand Synthesis System (Invitrogen) according to the manufacturer's instructions. TaqMan Gene Expression Assays and TaqMan Gene Expression Master Mix (Applied Biosystems) were used on a Bio-Rad CFX96 thermocycler with the following protocol: 50°C for 2 min; 95°C for 10 min; 40 cycles of 95°C for 15 s and 60°C for 1 min. Target genes were normalized to RPS18 expression, and relative gene expression was calculated using the comparative ▲Ct method. When fold differences are calculated and compared, RNA for each condition was collected in biologic triplicate and assayed in technical replicate and fold change (2^-▲Ct) in relative mRNA expression levels of target genes. Values are reported for each gene with SDs after testing for the data's lognormal distribution. Statistical analysis was conducted using GraphPad Prism software. Significance was determined using a one-way analysis of variance (ANOVA) with Tukey-Kramer post hoc test for multiple comparisons at a 95% confidence threshold.

Western Blot

SCRIB protein expression was qualitatively confirmed in the WA09 parent and P1043L mutant clones, and its absence was confirmed in the KO mutant clone via western blotting. Briefly, NEC monolayers derived in 6-well plates were pelleted and lysed in RIPA buffer (Thermo Fisher Scientific 89900) containing protease inhibitors (Thermo Fisher Scientific 78429) and stored at -80 °C. Upon thaw, lysates were analyzed for total protein concentration using the Lowry protein assay (Biorad DC Protein Assay). 25 µg of protein was analyzed on a 4-20% Mini-PROTEAN® TGX™ Precast Gel (Bio-Rad, 4561094) and transferred to polyvinylidene fluoride (PVDF) membranes (Thermo Scientific 88518). The membranes were cut to separate the 215 kDa SCRIB protein from the 50 kDA B-tubulin housekeeping protein and blotted overnight at 4ºC with an anti-SCRIB antibody (1:500; Invitrogen PA5-54821) or Anti-β-tubulin (BioLegend 1:500),

respectively. Washes were conducted the next day, and membranes were incubated in horseradish peroxidase-conjugated goat anti-rabbit at room temperature, followed by addition of enhanced chemiluminescence (ECL) substrate (made in-house). Membranes were visualized using a chemiluminescence imager (DNR Bio-Imaging Systems) at 10 second intervals, ~100s total exposure.

Quantification and Statistical Analysis

GraphPad Prism (V10.2.1) was used for all statistical analysis. Error bars represent mean ± SD; * for $p<0.05$, ** for $p<0.01$, *** for $p<0.001$, **** for $p<0.0001$. Neural rosette emergence for single dose experiments were analyzed with t-tests and all other metrics were analyzed with One-way ANOVAs. Non-linear regression was performed to generate three (Hill Slope =1) or four (Hill Slope not restrained) parameter dose-response curves depending on whether data points were present at the curve's inflection point. Comparison of dose-response curves for different metrics analyzing the same compound were compared using a hypothetical dose-response curve for all metrics. The explanation of "n" and the number of technical or biological replicates completed per experiment, as well as tests done to determine if data met assumptions of statistical approaches, can be found in the figure legends and text.

FIGURE LEGENDS

Figure 1. FB and SC RosetteArrays derived from cryopreserved cell banks. (A) Schematic of 12-well plate format used for direct seeding of cryopreserved hPSCs and cervical spinal NMPs onto micropatterned substrates. (B) Image of resultant immunostained FB RosetteArray showing singularly polarized (N-cadherin$^+$) neural rosette formation. (C) Culture schema for FB and SC RosetteArrays derivation with (D) images showing distinct FB (i) and SC (ii) rosette tissue morphologies. (E) Dot plot of RosetteArray derivation in E6 media supplemented with up to 0.1% v/v DMSO. Each data point is the average of a single experiment (n=50 tissues per well). (F) Time course images of micropatterned rosette tissue morphogenesis at Day (D) 3-6 of FB RosetteArray derivation. Scale bars: x = 125 µm; z = 45 µm. (G) Plot tracking polarized N-cadherin ring's profile (xz-plane) shape, i.e.,'Flat' vs. 'Curled' vs. 'Ring', to document 2- to 3-D rosette tissue morphogenesis. Each data point is the average of a single experiment, n = 40 tissues per well. Scale bars are (b) 250 and (d)100 µm. 1-way ANOVA with Tukey-Kramer post-hoc analysis; *$p \leq 0.05$, **$p \leq 0.01$, *** $p \leq 0.001$, **** $p \leq 0.0001$.

Figure 2. Dose-response of FB RosetteArrays exposed to Glycolic Acid, Benomyl, Valproic Acid, Methotrexate, and Novobiocin. Glycolic acid dose-response graphs display percent %inhibition of (A) Cells/Tissue, (B) %Pax6 expression, and (C) single rosette emergence (Rosettes) plus (D) a composite dose-response curve overlay (Blue-Cells/Tissue, Red-%Pax6, and Green-Rosettes). This is repeated for Benomyl (E-H), Valproic Acid (I-L), Methotrexate (M-P), and Novobiocin (Q-T). Each dose point is the average of a technical triplicate, n=50 tissues per well. Three-parameter non-linear regression used to model and compare each metric.

Figure 3. RosetteArrays display region-specific responses to VPA exposure. (A) Culture schema for SC RosetteArray VPA dose-response experiments with (B) representative images of immunostained FB and SC rosettes. Comparison of FB and SC RosetteArray dose-response curves for %inhibition of (C) Cells/Tissue, (D) %Pax6 expression, and (E) single rosette emergence (Rosettes) as well as (F) measured N-cadherin$^+$ polarized ring area. Technical triplicates for each dose, n=50 tissues/well. Three parameter non-linear regression used to model and compare each metric. Scale bars are 100 µm.

Figure 4. FB RosetteArrays can integrate simulated human metabolism and provide DNT assessment. RosetteArray classification for 29 select DNT compounds screened at 10 µM and with human S9 pooled-liver fraction pre-digestion for their ability to perturb cell viability/proliferation, neural differentiation, and rosette morphogenesis and area. Color coded summary: 'Negative', no effect - green; 'Warning', significant decrease < 25% - dotted red; 'Positive' hit, significant decrease >25% - red; not analyzed – grey. Technical triplicate, n=50 tissues/well. Comparison of the FB RosetteArray's 'Assay Classification' versus the compound's 'Referenced Classification' from literature review is also provided. TN – true negative, TP – true positive, FN – false negative, FP – false positive. Non-metabolized compared to control via two-tailed T-test. Metabolized compared via one-way ANOVA. *$p \leq 0.05$.

Figure 5. FB and SC RosetteArray assay and analysis scale-up to 96-well plate format. (A) Schematic of 96-well RosetteArray plate manufacture, image acquisition, and RosetteDetect image analysis. Quantification of (B-E) FB and (F-I) cervical spinal 96-well RosetteArrays with and without 0.1% DMSO across differentiation Days 5-7 for (B, F) cells/tissue, (C, G) neural induction, and (D, H) rosette emergence plus (E, I) representative immunostaining. Quantification of Day 5 lumbar spinal RosetteArrays with 0.1% DMSO at varied seeding density for (J) cells/tissue, (K) neural induction, and (L) rosette emergence plus (M) representative immunostaining. Dose-response curves for manually and RosetteDetect quantified FB RosetteArray assays of (N) Aspirin, (O) Permethrin, and (P) Rotenone. Each data point represents an average across 2-4 technical replicates with n=40 analyzed tissues per well. Scale bars are 100 µm. Significance in dot plots assessed using 1-way ANOVA with Tukey-Kramer post-hoc analysis, * $p \leq 0.05$. Dose-response curves compared using three-parameter non-linear regression models. If curves are statistically equivalent, then only one curve is displayed.

Figure 6. FB and SC RosetteArrays detect folate metabolic pathway-specific risk with regional differences. (A) Culture schema for MTX/DTG exposure with 5-MTHFA rescue in 12-well FB RosetteArrays. (B) Inhibitory effect of 1.0 µM MTX on FB rosette emergence and rescue using concurrent 20.0 µM 5-MTHFA treatment. Quantification of MTX dose-response on 12-well FB RosetteArray derivation with 20.0 µM 5-MTHFA treatment across (C) cells/tissue, (D) neural induction, (E) single rosette emergence, and (F) rosette area metrics. Quantification of DTG's inhibitory effects on 12-well FB RosetteArray derivation with increasing 5-MTHFA supplementation across (H) cells/tissue, (I), neural induction, (J) single rosette emergence, and (K) rosette area metrics. (L) Culture schema for MTX dose-response comparison between 96-well FB and lumbar SC RosetteArrays. Dose-response curves of %inhibition of (M) cells/tissue (N) neural induction, and (O) single rosette emergence. (C-F, H-K) Each data point is the average of technical triplicate, n=50 tissues analyzed per well. (C-F) Three-parameter non-linear regression used to model and compare each metric. (H-K) Significance assessed using 1-way ANOVA with Tukey-Kramer post-hoc analysis, * $p \leq 0.05$. (M-O) Each data point is the average of two biological replicates, each dose in technical quadruplicate, n=40 tissues analyzed per well. Four-parameter non-linear regression used to model and compare each metric. If curves are statistically equivalent, then only one curve is displayed. Scale bars are 100 µm.

Figure 7. RosetteArrays detect clinically relevant genetic and multifactorial NTD risks. (A) Culture schema for (B) initial and (C) secondary FB RosetteArray MTX dose-response comparison of single rosette emergence across *MTHFR*$^{C677T(-/-)}$ and SCRIB$^{P1043L(-/-)}$/*MTHFR*$^{C677T(+/-)}$ mutant lines and the WA09 *MTHFR*$^{C677T(+/-)}$ isogenic control. (D) Culture schema for 5-MTHFA dose-response rescue of *MTHFR*$^{C677T(-/-)}$ mutant and the WA09 *MTHFR*$^{C677T(+/-)}$ isogenic control under 1 µM MTX exposure with (E) representative staining and (F)

quantification of %normalized single rosette emergence. Each data point on a dose-response curve is the average of technical quadruplicate, n=40 tissues analyzed per well. Four-parameter non-linear regression used to model and compare each metric. (G) Culture schema for FB and cervical SC RosetteArrays of $SCRIB^{P1043L(+/-)}$, $SCRIB^{P1043L(-/-)}$, $SCRIB^{KO}$ mutant lines with (H) representative immunostaining and FB (I-K) and SC (L-N) quantification for cells viability/proliferation, neural induction, and %single rosette emergence. Data represents two biologic replicates with n=6-7 technical replicates total. Data is compared via a 1-way ANOVA with Tukey-Kramer post-hoc analysis. **** $p \leq 0.0001$. Scale bars are 100 µm.

1. Lancaster, M. A., Renner, M., Martin, C.-A., Wenzel, D., Bicknell, L. S., Hurles, M. E., Homfray, T., Penninger, J. M., Jackson, A. P. & Knoblich, J. A. Cerebral organoids model human brain development and microcephaly. *Nature* **501,** 373–379 (2013).

2. Pollen, A. A., Bhaduri, A., Andrews, M. G., Nowakowski, T. J., Meyerson, O. S., Mostajo-Radji, M. A., Lullo, E. D., Alvarado, B., Bedolli, M., Dougherty, M. L., Fiddes, I. T., Kronenberg, Z. N., Shuga, J., Leyrat, A. A., West, J. A., Bershteyn, M., Lowe, C. B., Pavlovic, B. J., Salama, S. R., Haussler, D., Eichler, E. E. & Kriegstein, A. R. Establishing Cerebral Organoids as Models of Human-Specific Brain Evolution. *Cell* **176,** 743-756.e17 (2019).

3. Bershteyn, M., Nowakowski, T. J., Pollen, A. A., Lullo, E. D., Nene, A., Wynshaw-Boris, A. & Kriegstein, A. R. Human iPSC-Derived Cerebral Organoids Model Cellular Features of Lissencephaly and Reveal Prolonged Mitosis of Outer Radial Glia. *Cell Stem Cell* **20,** 435–449 (2017).

4. Eze, U. C., Bhaduri, A., Haeussler, M., Nowakowski, T. J. & Kriegstein, A. R. Single-cell atlas of early human brain development highlights heterogeneity of human neuroepithelial cells and early radial glia. *Nature Neuroscience* **24,** 584–594 (2021).

5. Atamian, A., Birtele, M., Hosseini, N., Nguyen, T., Seth, A., Dosso, A. D., Paul, S., Tedeschi, N., Taylor, R., Coba, M. P., Samarasinghe, R., Lois, C. & Quadrato, G. Human cerebellar organoids with functional Purkinje cells. *Cell Stem Cell* **31,** 39-51.e6 (2024).

6. Phillips, M. J., Wallace, K. A., Dickerson, S. J., Miller, M. J., Verhoeven, A. D., Martin, J. M., Wright, L. S., Shen, W., Capowski, E. E., Percin, E. F., Perez, E. T., Zhong, X., Canto-Soler, M. V. & Gamm, D. M. Blood-Derived Human iPS Cells Generate Optic Vesicle–Like Structures with the Capacity to Form Retinal Laminae and Develop Synapses. *Investig. Opthalmology Vis. Sci.* **53,** 2007 (2012).

7. Ogura, T., Sakaguchi, H., Miyamoto, S. & Takahashi, J. Three-dimensional induction of dorsal, intermediate and ventral spinal cord tissues from human pluripotent stem cells. *Development* **145,** (2018).

8. Jo, J., Xiao, Y., Sun, A. X., Cukuroglu, E., Tran, H.-D., Göke, J., Tan, Z. Y., Saw, T. Y., Tan, C.-P., Lokman, H., Lee, Y., Kim, D., Ko, H. S., Kim, S.-O., Park, J. H., Cho, N.-J., Hyde, T. M., Kleinman, J. E., Shin, J. H., Weinberger, D. R., Tan, E. K., Je, H. S. & Ng, H.-H. Midbrain-like

Organoids from Human Pluripotent Stem Cells Contain Functional Dopaminergic and Neuromelanin-Producing Neurons. *Cell Stem Cell* **19,** 248–257 (2016).

9. Vandana, J. J., Manrique, C., Lacko, L. A. & Chen, S. Human pluripotent-stem-cell-derived organoids for drug discovery and evaluation. *Cell Stem Cell* **30,** 571–591 (2023).

10. Andrews, M. G. & Kriegstein, A. R. Challenges of Organoid Research. *Annu. Rev. Neurosci.* **45,** 1–17 (2022).

11. Fedorchak, N. J., Iyer, N. & Ashton, R. S. Bioengineering tissue morphogenesis and function in human neural organoids. *Seminars in Cell & Developmental Biology* (2020). doi:10.1016/j.semcdb.2020.05.025

12. Wallingford, J. B., Niswander, L. A., Shaw, G. M. & Finnell, R. H. The continuing challenge of understanding, preventing, and treating neural tube defects. *Science (New York, N.Y.)* **339,** 1047 (2013).

13. Aguiar-Pulido, V., Wolujewicz, P., Martinez-Fundichely, A., Elhaik, E., Thareja, G., Aleem, A. A., Chalhoub, N., Cuykendall, T., Al-Zamer, J., Lei, Y., El-Bashir, H., Musser, J. M., Al-Kaabi, A., Shaw, G. M., Khurana, E., Suhre, K., Mason, C. E., Elemento, O., Finnell, R. H. & Ross, M. E. Systems biology analysis of human genomes points to key pathways conferring spina bifida risk. *P Natl Acad Sci Usa* **118,** e2106844118 (2021).

14. Paulsen, B., Velasco, S., Kedaigle, A. J., Pigoni, M., Quadrato, G., Deo, A. J., Adiconis, X., Uzquiano, A., Sartore, R., Yang, S. M., Simmons, S. K., Symvoulidis, P., Kim, K., Tsafou, K., Podury, A., Abbate, C., Tucewicz, A., Smith, S. N., Albanese, A., Barrett, L., Sanjana, N. E., Shi, X., Chung, K., Lage, K., Boyden, E. S., Regev, A., Levin, J. Z. & Arlotta, P. Autism genes converge on asynchronous development of shared neuron classes. *Nature* **602,** 268–273 (2022).

15. Bai, D., Yip, B. H. K., Windham, G. C., Sourander, A., Francis, R., Yoffe, R., Glasson, E., Mahjani, B., Suominen, A., Leonard, H., Gissler, M., Buxbaum, J. D., Wong, K., Schendel, D., Kodesh, A., Breshnahan, M., Levine, S. Z., Parner, E. T., Hansen, S. N., Hultman, C., Reichenberg, A. & Sandin, S. Association of Genetic and Environmental Factors With Autism in a 5-Country Cohort. *JAMA Psychiatry* **76,** 1035–1043 (2019).

16. Notaras, M., Lodhi, A., Dündar, F., Collier, P., Sayles, N. M., Tilgner, H., Greening, D. & Colak, D. Schizophrenia is defined by cell-specific neuropathology and multiple neurodevelopmental mechanisms in patient-derived cerebral organoids. *Mol. Psychiatry* **27,** 1416–1434 (2022).

17. Felice, A. D., Ricceri, L., Venerosi, A., Chiarotti, F. & Calamandrei, G. Multifactorial Origin of Neurodevelopmental Disorders: Approaches to Understanding Complex Etiologies. *Toxics* **3,** 89–129 (2015).

18. Chen, G. T. & Geschwind, D. H. Challenges and opportunities for precision medicine in neurodevelopmental disorders. *Adv. drug Deliv. Rev.* **191,** 114564–114564 (2022).

19. Eiraku, M., Watanabe, K., Matsuo-Takasaki, M., Kawada, M., Yonemura, S., Matsumura, M., Wataya, T., Nishiyama, A., Muguruma, K. & Sasai, Y. Self-organized formation of polarized cortical tissues from ESCs and its active manipulation by extrinsic signals. *Cell Stem Cell* **3,** 519–532 (2008).

20. Birtele, M., Dosso, A. D., Xu, T., Nguyen, T., Wilkinson, B., Hosseini, N., Nguyen, S., Urenda, J.-P., Knight, G., Rojas, C., Flores, I., Atamian, A., Moore, R., Sharma, R., Pirrotte, P., Ashton, R. S., Huang, E. J., Rumbaugh, G., Coba, M. P. & Quadrato, G. Non-synaptic function of the autism spectrum disorder-associated gene SYNGAP1 in cortical neurogenesis. *Nat. Neurosci.* **26,** 2090–2103 (2023).

21. Knight, G. T., Lundin, B. F., Iyer, N., Ashton, L. M., Sethares, W. A., Willett, R. M. & Ashton, R. S. Engineering induction of singular neural rosette emergence within hPSC-derived tissues. *eLife* **7,** e37549 (2018).

22. Iyer, N. R., Shin, J., Cuskey, S., Tian, Y., Nicol, N. R., Doersch, T. E., Seipel, F., McCalla, S. G., Roy, S. & Ashton, R. S. Modular derivation of diverse, regionally discrete human posterior CNS neurons enables discovery of transcriptomic patterns. *Sci Adv* **8,** (2022).

23. Wang, Y., Chiola, S., Yang, G., Russell, C., Armstrong, C. J., Wu, Y., Spampanato, J., Tarboton, P., Ullah, H. M. A., Edgar, N. U., Chang, A. N., Harmin, D. A., Bocchi, V. D., Vezzoli, E., Besusso, D., Cui, J., Cattaneo, E., Kubanek, J. & Shcheglovitov, A. Modeling human telencephalic development and autism-associated SHANK3 deficiency using organoids generated from single neural rosettes. *Nat Commun* **13,** 5688 (2022).

24. Tidball, A. M., Niu, W., Ma, Q., Takla, T. N., Walker, J. C., Margolis, J. L., Mojica-Perez, S. P., Sudyk, R., Deng, L., Moore, S. J., Chopra, R., Shakkottai, V. G., Murphy, G. G., Yuan, Y., Isom, L. L., Li, J. Z. & Parent, J. M. Deriving early single-rosette brain organoids from human pluripotent stem cells. *Stem Cell Rep.* (2023). doi:10.1016/j.stemcr.2023.10.020

25. Karzbrun, E., Khankhel, A. H., Megale, H. C., Glasauer, S. M. K., Wyle, Y., Britton, G., Warmflash, A., Kosik, K. S., Siggia, E. D., Shraiman, B. I. & Streichan, S. J. Human neural tube morphogenesis in vitro by geometric constraints. *Nature* 1–5 (2021). doi:10.1038/s41586-021-04026-9

26. Haremaki, T., Metzger, J. J., Rito, T., Ozair, M. Z., Etoc, F. & Brivanlou, A. H. Self-organizing neuruloids model developmental aspects of Huntington's disease in the ectodermal compartment. *Nature Biotechnology* **37,** 1198–1208 (2019).

27. Xue, X., Kim, Y. S., Ponce-Arias, A.-I., O'Laughlin, R., Yan, R. Z., Kobayashi, N., Tshuva, R. Y., Tsai, Y.-H., Sun, S., Zheng, Y., Liu, Y., Wong, F. C. K., Surani, A., Spence, J. R., Song, H., Ming, G.-L., Reiner, O. & Fu, J. A Patterned Human Neural Tube Model Using Microfluidic Gradients. *Nature* 1–3 (2024). doi:10.1038/s41586-024-07204-7

28. Lippmann, E. S., Williams, C. E., Ruhl, D. A., Estevez-Silva, M. C., Chapman, E. R., Coon, J. J. & Ashton, R. S. Deterministic HOX patterning in human pluripotent stem cell-derived neuroectoderm. *Stem Cell Reports* **4,** 632–644 (2015).

29. Lippmann, E. S., Estevez-Silva, M. C. & Ashton, R. S. Defined human pluripotent stem cell culture enables highly efficient neuroepithelium derivation without small molecule inhibitors. *Stem cells (Dayton, Ohio)* **32,** 1032–1042 (2014).

30. Dreser, N., Madjar, K., Holzer, A.-K., Kapitza, M., Scholz, C., Kranaster, P., Gutbier, S., Klima, S., Kolb, D., Dietz, C., Trefzer, T., Meisig, J., Thriel, C. van, Henry, M., Berthold, M. R., Blüthgen, N., Sachinidis, A., Rahnenführer, J., Hengstler, J. G., Waldmann, T. & Leist, M. Development of a neural rosette formation assay (RoFA) to identify neurodevelopmental toxicants and to characterize their transcriptome disturbances. *Archives of toxicology* **34,** 49–21 (2019).

31. Miranda, C. C., Fernandes, T. G., Pinto, S. N., Prieto, M., Diogo, M. M. & Cabral, J. M. S. A scale out approach towards neural induction of human induced pluripotent stem cells for neurodevelopmental toxicity studies. *Toxicology Letters* **294,** 51–60 (2018).

32. Jourdon, A., Wu, F., Mariani, J., Capauto, D., Norton, S., Tomasini, L., Amiri, A., Suvakov, M., Schreiner, J. D., Jang, Y., Panda, A., Nguyen, C. K., Cummings, E. M., Han, G., Powell, K., Szekely, A., McPartland, J. C., Pelphrey, K., Chawarska, K., Ventola, P., Abyzov, A. & Vaccarino, F. M. Modeling idiopathic autism in forebrain organoids reveals an imbalance of excitatory cortical neuron subtypes during early neurogenesis. *Nat. Neurosci.* 1–11 (2023). doi:10.1038/s41593-023-01399-0

33. Hendricks, E., Quihuis, A. M., Hung, S.-T., Chang, J., Dorjsuren, N., Der, B., Staats, K. A., Shi, Y., Maria, N. S. S., Jacobs, R. E. & Ichida, J. K. The C9ORF72 repeat expansion alters neurodevelopment. *Cell Rep.* **42,** 112983 (2023).

34. Miotto, M., Rosito, M., Paoluzzi, M., Turris, V. de, Folli, V., Leonetti, M., Ruocco, G., Rosa, A. & Gosti, G. Collective behavior and self-organization in neural rosette morphogenesis. *Front. Cell Dev. Biol.* **11,** 1134091 (2023).

35. Lee, J.-H., Shin, H., Shaker, M. R., Kim, H. J., Park, S.-H., Kim, J. H., Lee, N., Kang, M., Cho, S., Kwak, T. H., Kim, J. W., Song, M.-R., Kwon, S.-H., Han, D. W., Lee, S., Choi, S.-Y., Rhyu, I. J., Kim, H., Geum, D., Cho, I.-J. & Sun, W. Production of human spinal-cord organoids recapitulating neural-tube morphogenesis. *Nat Biomed Eng* 1–14 (2022). doi:10.1038/s41551-022-00868-4

36. Iskandar, B. J. & Finnell, R. H. Spina Bifida. *New Engl J Med* **387,** 444–450 (2022).

37. Copp, A. J., Greene, N. D. E. & Murdoch, J. N. The genetic basis of mammalian neurulation. *Nature Reviews Genetics* **4,** 784–793 (2003).

38. MVSR Group. Prevention of neural tube defects: results of the Medical Research Council Vitamin Study. *The Lancet* **338,** 131–137 (1991).

39. Hanson, C. & Caisander, G. Human embryonic stem cells and chromosome stability. *APMIS* **113,** 751–755 (2005).

40. Zhang, X., Huang, C. T., Chen, J., Pankratz, M. T., Xi, J., Li, J., Yang, Y., Lavaute, T. M., Li, X.-J., Ayala, M., Bondarenko, G. I., Du, Z.-W., Jin, Y., Golos, T. G. & Zhang, S.-C. Pax6 is a human neuroectoderm cell fate determinant. *Cell Stem Cell* **7,** 90–100 (2010).

41. Chetty, S., Pagliuca, F. W., Honore, C., Kweudjeu, A., Rezania, A. & Melton, D. A. A simple tool to improve pluripotent stem cell differentiation. *Nat Methods* **10,** 553–556 (2013).

42. Li, J., Narayanan, C., Bian, J., Sambo, D., Brickler, T., Zhang, W. & Chetty, S. A transient DMSO treatment increases the differentiation potential of human pluripotent stem cells through the Rb family. *PLoS ONE* **13,** e0208110 (2018).

43. Daston, G. P., Beyer, B. K., Carney, E. W., Chapin, R. E., Friedman, J. M., Piersma, A. H., Rogers, J. M. & Scialli, A. R. Exposure-Based Validation List for Developmental Toxicity Screening Assays. *Birth defects research. Part B, Developmental and reproductive toxicology* **101,** 423–428 (2014).

44. Rull, R. P., Ritz, B. & Shaw, G. M. Neural Tube Defects and Maternal Residential Proximity to Agricultural Pesticide Applications. *American Journal of Epidemiology* **163,** 743–753 (2006).

45. Nishimura, T., Honda, H. & Takeichi, M. Planar cell polarity links axes of spatial dynamics in neural-tube closure. *Cell* **149,** 1084–1097 (2012).

46. Lammer, E. J., Sever, L. E. & Oakley, G. P. Teratogen Update - Valproic Acid. *Teratology* **35,** 465–473 (1987).

47. Hughes, A., Greene, N. D. E., Copp, A. J. & Galea, G. L. Valproic acid disrupts the biomechanics of late spinal neural tube closure in mouse embryos. *Mechanisms of development* **149,** 20–26 (2018).

48. Fleming, A. & Copp, A. J. Embryonic Folate Metabolism and Mouse Neural Tube Defects. *Science* **280,** 2107–2109 (1998).

49. Warkany, J. Aminopterin and Methotrexate - Folic-Acid Deficiency. *Teratology* **17,** 353–357 (1978).

50. Hunter, M. C., O'Hagan, K. L., Kenyon, A., Dhanani, K. C. H., Prinsloo, E. & Edkins, A. L. Hsp90 Binds Directly to Fibronectin (FN) and Inhibition Reduces the Extracellular Fibronectin Matrix in Breast Cancer Cells. *PLoS ONE* **9,** e86842 (2014).

51. Balashova, O. A., Panoutsopoulos, A. A., Visina, O., Selhub, J., Knoepfler, P. S. & Borodinsky, L. N. Noncanonical function of folate through folate receptor 1 during neural tube formation. *Nat. Commun.* **15,** 1642 (2024).

52. Robert, E. & Guibaud, P. Maternal valproic acid and congenital neural tube defects. *Lancet* **320,** 937 (1982).

53. Lindhout, D. & Meinardi, H. Spina bifida and in-utero exposure to valproate. *Lancet* **324,** 396 (1984).

54. (EFSA), E. F. S. A., Arena, M., Auteri, D., Barmaz, S., Bellisai, G., Brancato, A., Brocca, D., Bura, L., Byers, H., Chiusolo, A., Marques, D. C., Crivellente, F., Lentdecker, C. D., Egsmose, M., Erdos, Z., Fait, G., Ferreira, L., Goumenou, M., Greco, L., Ippolito, A., Istace, F., Jarrah, S., Kardassi, D., Leuschner, R., Lythgo, C., Magrans, J. O., Medina, P., Miron, I., Molnar, T., Nougadere, A., Padovani, L., Morte, J. M. P., Pedersen, R., Reich, H., Sacchi, A., Santos, M., Serafimova, R., Sharp, R., Stanek, A., Streissl, F., Sturma, J., Szentes, C., Tarazona, J., Terron, A., Theobald, A., Vagenende, B., Verani, A. & Villamar□Bouza, L. Peer review of the pesticide risk assessment of the active substance desmedipham. *EFSA J.* **16,** e05150 (2018).

55. Therapontos, C., Erskine, L., Gardner, E. R., Figg, W. D. & Vargesson, N. Thalidomide induces limb defects by preventing angiogenic outgrowth during early limb formation. *Proc. Natl. Acad. Sci.* **106,** 8573–8578 (2009).

56. Uibel, F. & Schwarz, M. Prediction of embryotoxic potential using the ReProGlo stem cell-based Wnt reporter assay. *Reproductive toxicology (Elmsford, N.Y.)* **55,** 30–49 (2015).

57. Saillenfait, A.-M., Sabaté, J.-P. & Gallissot, F. Comparative embryotoxicities of butyl benzyl phthalate, mono-n-butyl phthalate and mono-benzyl phthalate in mice and rats: in vivo and in vitro observations. *Reprod. Toxicol.* **17,** 575–583 (2003).

58. Davenport, C. E.P.A. to Block Pesticide Tied to Neurological Harm in Children. *New York TImes* (2018). at <https://www.nytimes.com/2021/08/18/climate/pesticides-epa-chlorpyrifos.html>;

59. Solomon, G. Reasons Why California Is Banning Chlorpyrifos, A Widely Used Pesticide | Best States | US News.pdf. *US News & World Report* (2020). at <https://www.usnews.com/news/best-states/articles/2020-01-23/reasons-why-california-is-banning-chlorpyrifos-a-widely-used-pesticide>;

60. Cao, F., Souders, C. L., Li, P., Pang, S., Qiu, L. & Martyniuk, C. J. Developmental toxicity of the triazole fungicide cyproconazole in embryo-larval stages of zebrafish (Danio rerio). *Environ. Sci. Pollut. Res.* **26,** 4913–4923 (2019).

61. Padilla, S., Corum, D., Padnos, B., Hunter, D. L., Beam, A., Houck, K. A., Sipes, N., Kleinstreuer, N., Knudsen, T., Dix, D. J. & Reif, D. M. Zebrafish developmental screening of the ToxCast^{TM} Phase I chemical library. *Reproductive Toxicology* **33,** 174–187 (2012).

62. Silva, M. H. Investigating open access new approach methods (NAM) to assess biological points of departure: A case study with 4 neurotoxic pesticides. *Curr. Res. Toxicol.* **6,** 100156 (2024).

63. Mathur, J. & Chua, N.-H. Microtubule Stabilization Leads to Growth Reorientation in Arabidopsis Trichomes. *Plant Cell* **12,** 465–477 (2000).

64. European Food Safety Authority. Peer review of the pesticide risk assessment of the active substance propyzamide. *EFSA J.* **14,** (2016).

65. Harkness, T., McNulty, J. D., Prestil, R., Seymour, S. K., Klann, T., Murrell, M., Ashton, R. S. & Saha, K. High-content imaging with micropatterned multiwell plates reveals influence of cell geometry and cytoskeleton on chromatin dynamics. *Biotechnology journal* **10,** 1555–1567 (2015).

66. Li, Z., Liu, F., Yang, W., Peng, S. & Zhou, J. A Survey of Convolutional Neural Networks: Analysis, Applications, and Prospects. *IEEE Trans. Neural Netw. Learn. Syst.* **33,** 6999–7019 (2022).

67. Cabrera, R. M., Souder, J. P., Steele, J. W., Yeo, L., Tukeman, G., Gorelick, D. A. & Finnell, R. H. The antagonism of folate receptor by dolutegravir: developmental toxicity reduction by supplemental folic acid. *AIDS (London, England)* **33,** 1967–1976 (2019).

68. Zash, R., Makhema, J. & Shapiro, R. L. Neural-Tube Defects with Dolutegravir Treatment from the Time of Conception. *The New England journal of medicine* **379,** 979–981 (2018).

69. Zash, R., Holmes, L., Diseko, M., Jacobson, D. L., Brummel, S., Mayondi, G., Isaacson, A., Davey, S., Mabuta, J., Mmalane, M., Gaolathe, T., Essex, M., Lockman, S., Makhema, J. & Shapiro, R. L. Neural-Tube Defects and Antiretroviral Treatment Regimens in Botswana. *The New England journal of medicine* **381,** 827–840 (2019).

70. Tukeman, G. L., Wei, H., Lin, Y. L., Wlodarczyk, B. J., Finnell, R. H. & Cabrera, R. M. Dolutegravir-induced neural tube defects in mice are folate responsive. *AIDS* **38,** 439–446 (2024).

71. Juriloff, D. M. & Harris, M. J. Insights into the Etiology of Mammalian Neural Tube Closure Defects from Developmental, Genetic and Evolutionary Studies. *Journal of developmental biology* **6,** 22 (2018).

72. Van der Put, N., Steegers-Theunissen, R., Frosst, P., Trijbels, F., Eskes, T., Van den Heuvel, L. P., Mariman, E., den Heyer, M., Rozen, R. & Blom, H. J. Mutated Methylenetetrahydrofolate Reductase as a Risk Factor for Spina-Bifida. *Lancet* **346,** 1070–1071 (1995).

73. Lei, Y., Zhu, H., Duhon, C., Yang, W., Ross, M. E., Shaw, G. M. & Finnell, R. H. Mutations in Planar Cell Polarity Gene SCRIB Are Associated with Spina Bifida. *PLoS ONE* **8,** e69262-8 (2013).

74. Frosst, P., Blom, H. J., Milos, R., Goyette, P., Sheppard, C. A., Matthews, R. G., Boers, G. J. H., Heijer, M. den, Kluijtmans, L. A. J., Heuve, L. P. van den & Rozen, R. A candidate genetic risk factor for vascular disease: a common mutation in methylenetetrahydrofolate reductase. *Nat. Genet.* **10,** 111–113 (1995).

75. Lesko, A. C., Keller, R., Chen, P. & Sutherland, A. Scribble mutation disrupts convergent extension and apical constriction during mammalian neural tube closure. *Dev Biol* **478,** 59–75 (2021).

76. Robinson, A., Escuin, S., Doudney, K., Vekemans, M., Stevenson, R. E., Greene, N. D. E., Copp, A. J. & Stanier, P. Mutations in the planar cell polarity genes CELSR1 and SCRIB are associated with the severe neural tube defect craniorachischisis. *Hum. Mutat.* **33,** 440–447 (2012).

77. Jones, V. J., Greene, N. D. E. & Copp, A. J. Occult Spinal Dysraphism. 325–344 (2019). doi:10.1007/978-3-030-10994-3_21

78. Boëda, B. & Etienne-Manneville, S. Spectrin binding motifs regulate Scribble cortical dynamics and polarity function. *eLife* **4,** e04726 (2015).

79. FDA, U. S. *Advancing New Alternative Methodologies at FDA January 2021*. 1–34 (2021). at <https://www.fda.gov/science-research/advancing-alternative-methods-fda/alternative-methods-publications-and-events>;

80. Thomas, R. S., Paules, R. S., Simeonov, A., Fitzpatrick, S. C., Crofton, K. M., Casey, W. M. & Mendrick, D. L. The US Federal Tox21 Program: A strategic and operational plan for continued leadership. *ALTEX* **35,** 163–168 (2018).

81. Committee, C. and B. *Initial Recommendations on Evaluation of Data from the Developmental Neurotoxicity (DNT) In-Vitro Testing Battery*. (Organization for Economic Co-operation and Development, 2023). at <https://www.oecd.org/env/ehs/testing/developmental-neurotoxicity.htm>;

82. Wu, Y., Peng, S., Finnell, R. H. & Zheng, Y. Organoids as a new model system to study neural tube defects. *The FASEB Journal* **35,** e21545 (2021).

83.Organization for Economic Co-operation and Development (OECD). *Test No. 426: Developmental Neurotoxicity Study*. (2007).

84. Tabatabaei, R. S., Fatahi-Meibodi, N., Meibodi, B., Javaheri, A., Abbasi, H., Hadadan, A., Bahrami, R., Mirjalili, S. R., Karimi-Zarchi, M. & Neamatzadeh, H. Association of Fetal MTHFR C677T Polymorphism with Susceptibility to Neural Tube Defects: A Systematic Review and Update Meta-Analysis. *Fetal and pediatric pathology* 1–17 (2020). doi:10.1080/15513815.2020.1775734

85. Copp, A. J. & Greene, N. D. E. Neural tube defects-disorders of neurulation and related embryonic processes. *Wiley interdisciplinary reviews. Developmental biology* **2,** 213–227 (2013).

86. Haeussler, M., Schönig, K., Eckert, H., Eschstruth, A., Mianné, J., Renaud, J.-B., Schneider-Maunoury, S., Shkumatava, A., Teboul, L., Kent, J., Joly, J.-S. & Concordet, J.-P. Evaluation of off-target and on-target scoring algorithms and integration into the guide RNA selection tool CRISPOR. *Genome Biol*. **17,** 148 (2016).

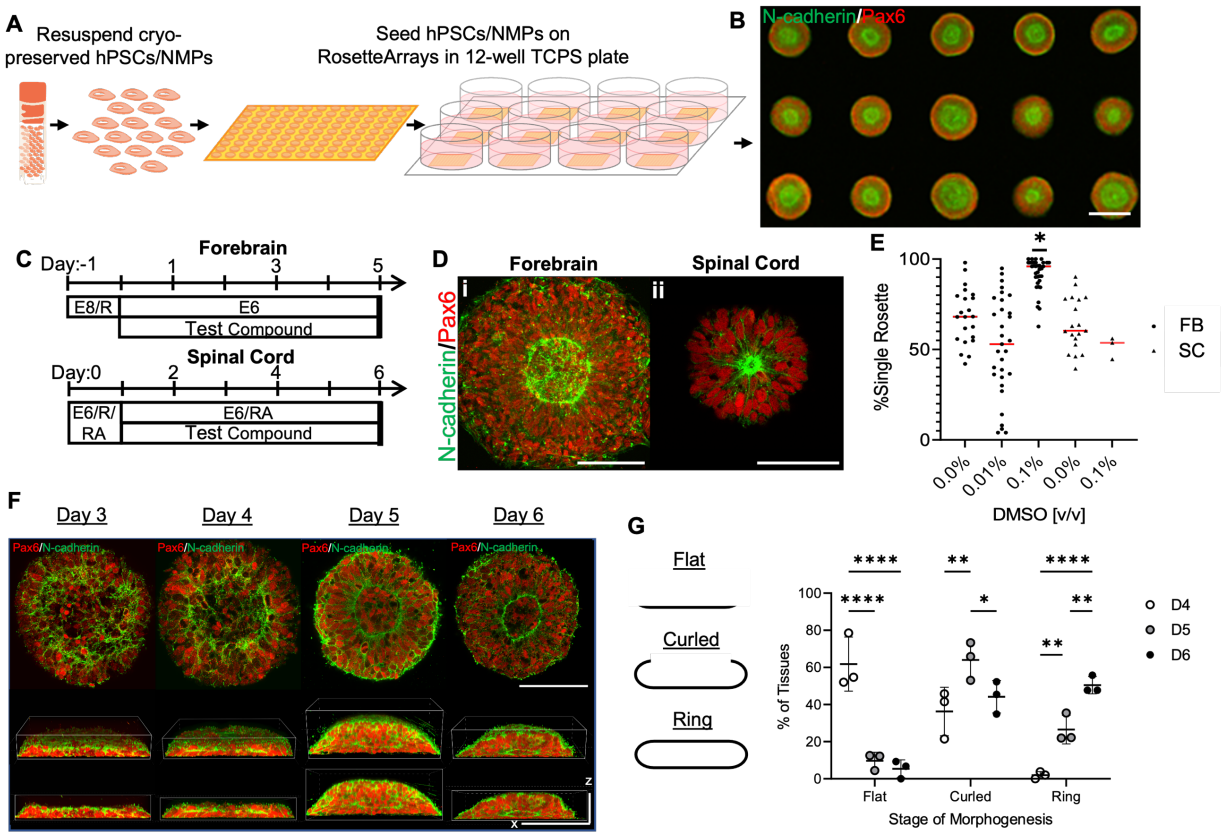

Figure 1. FB and SC RosetteArrays derived from cryopreserved cell banks. (A) Schematic of 12-well plate format used for direct seeding of cryopreserved hPSCs and cervical spinal NMPs onto micropatterned substrates. (B) Image of resultant immunostained FB RosetteArray showing singularly polarized (N-cadherin^{+}) neural rosette formation. (C) Culture schema for FB and SC RosetteArrays derivation with (D) images showing distinct FB (i) and SC (ii) rosette tissue morphologies. (E) Dot plot of RosetteArray derivation in E6 media supplemented with up to 0.1% v/v DMSO. Each data point is the average of a single experiment (n=50 tissues per well). (F) Time course images of micropatterned rosette tissue morphogenesis at Day (D) 3-6 of FB RosetteArray derivation. Scale bars: x = 125 µm; z = 45 µm. (G) Plot tracking polarized N-cadherin ring's profile (xz-plane) shape, i.e.,'Flat' vs. 'Curled' vs. 'Ring', to document 2- to 3-D rosette tissue morphogenesis. Each data point is the average of a single experiment, n = 40 tissues per well. Scale bars are (b) 250 and (d)100 µm. 1-way ANOVA with Tukey-Kramer post-hoc analysis; *$p \leq 0.05$, **$p \leq 0.01$, *** $p \leq 0.001$, **** $p \leq 0.0001$.

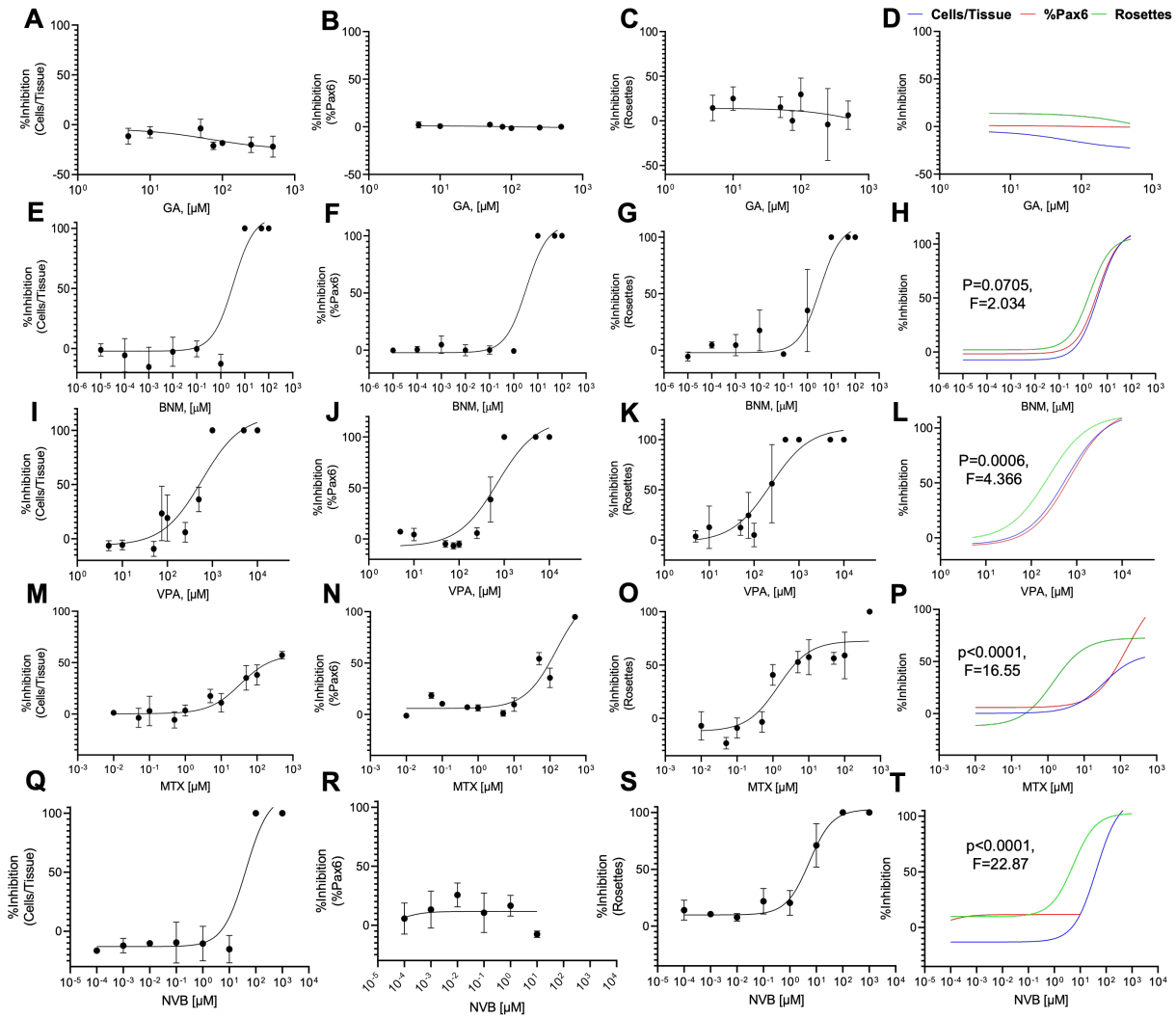

Figure 2. Dose-response of FB RosetteArrays exposed to Glycolic Acid, Benomyl, Valproic Acid, Methotrexate, and Novobiocin. Glycolic acid dose-response graphs display percent %inhibition of (A) Cells/Tissue, (B) %Pax6 expression, and (C) single rosette emergence (Rosettes) plus (D) a composite dose-response curve overlay (Blue-Cells/Tissue, Red-%Pax6, and Green-Rosettes). This is repeated for Benomyl (E-H), Valproic Acid (I-L), Methotrexate (M-P), and Novobiocin (Q-T). Each dose point is the average of a technical triplicate, n=50 tissues per well. Three-parameter non-linear regression used to model and compare each metric.

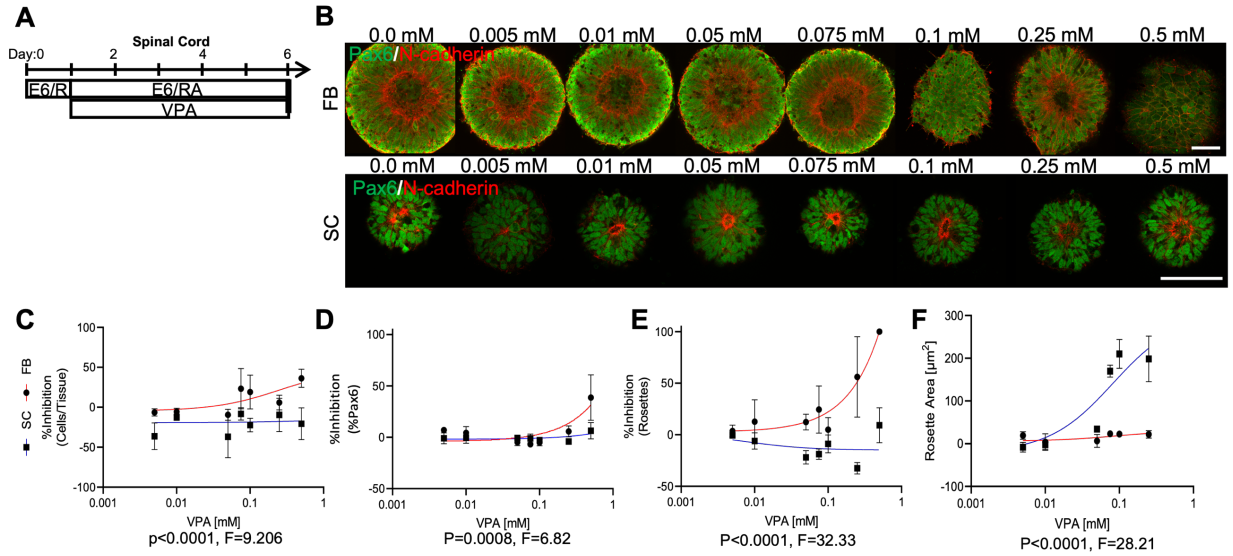

Figure 3. RosetteArrays display region-specific responses to VPA exposure. (A) Culture schema for SC RosetteArray VPA dose-response experiments with (B) representative images of immunostained FB and SC rosettes. Comparison of FB and SC RosetteArray dose-response curves for %inhibition of (C) Cells/Tissue, (D) %Pax6 expression, and (E) single rosette emergence (Rosettes) as well as (F) measured N-cadherin^{+} polarized ring area. Technical triplicates for each dose, n=50 tissues/well. Three parameter non-linear regression used to model and compare each metric. Scale bars are 100 μm.

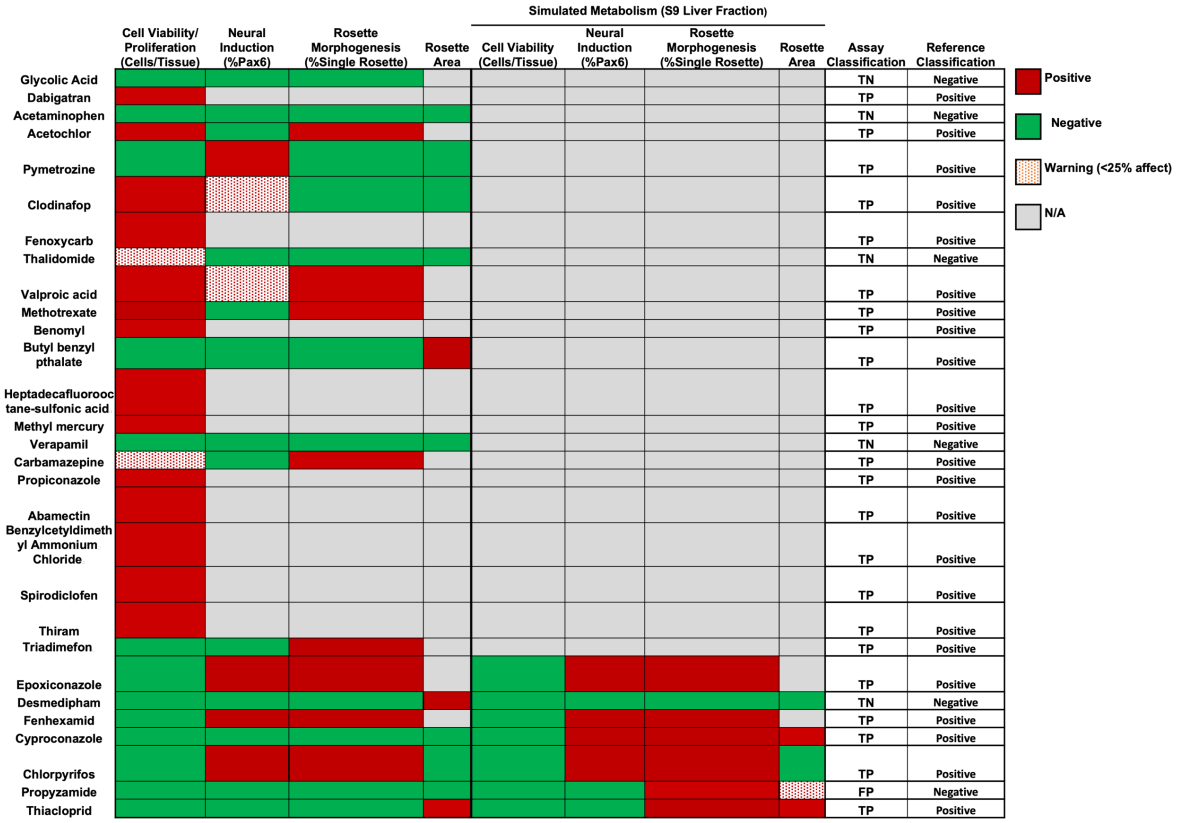

Figure 4. FB RosetteArrays can integrate simulated human metabolism and provide DNT assessment. RosetteArray classification for 29 select DNT compounds screened at 10 μM and with human S9 pooled-liver fraction pre-digestion for their ability to perturb cell viability/proliferation, neural differentiation, and rosette morphogenesis and area. Color coded summary: 'Negative', no effect - green; 'Warning', significant decrease < 25% - dotted red; 'Positive' hit, significant decrease >25% - red; not analyzed – grey. Technical triplicate, n=50 tissues/well. Comparison of the FB RosetteArray's 'Assay Classification' versus the compound's 'Referenced Classification' from literature review is also provided. TN – true negative, TP – true positive, FN – false negative, FP – false positive. Non-metabolized compared to control via two-tailed T-test. Metabolized compared via one-way ANOVA. *$p \leq 0.05$.

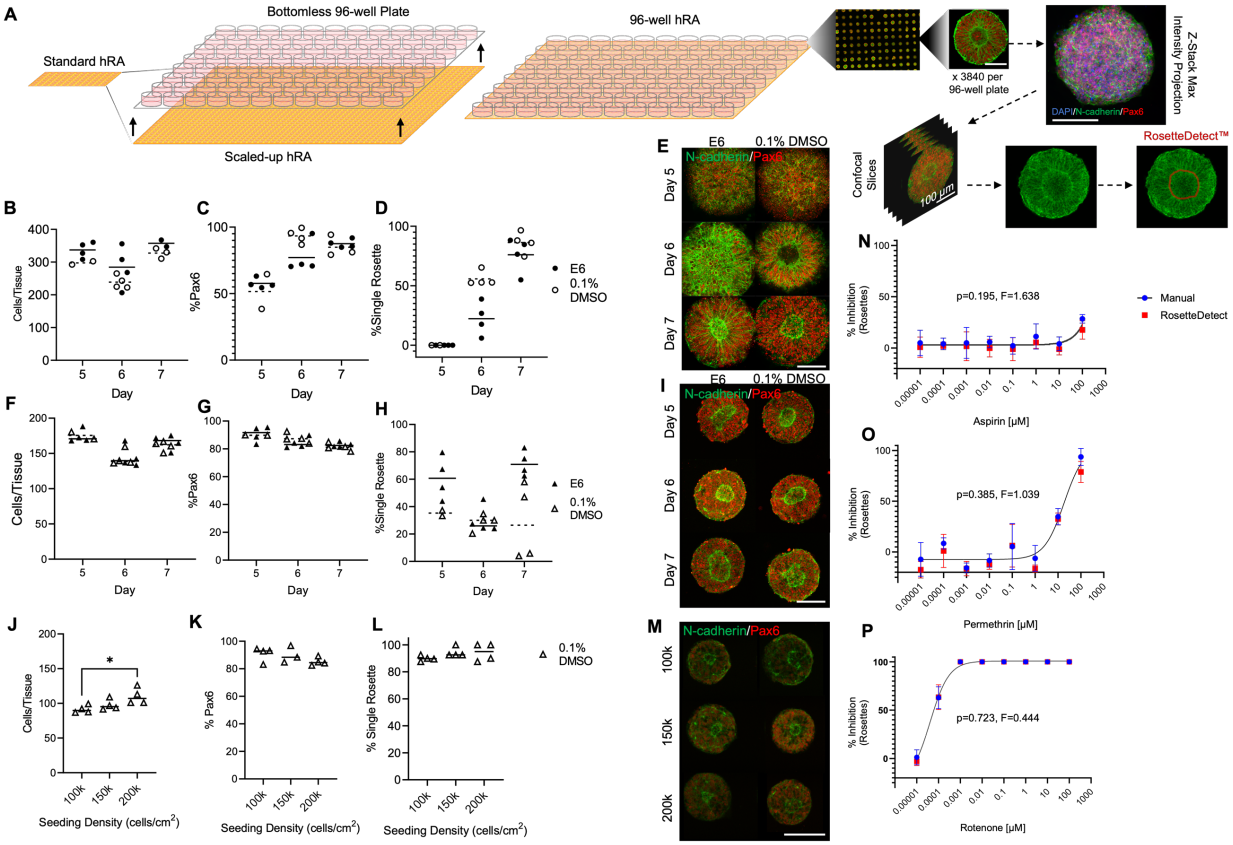

Figure 5. FB and SC RosetteArray assay and analysis scale-up to 96-well plate format. (A) Schematic of 96-well RosetteArray plate manufacture, image acquisition, and RosetteDetect image analysis. Quantification of (B-E) FB and (F-I) cervical spinal 96-well RosetteArrays with and without 0.1% DMSO across differentiation Days 5-7 for (B, F) cells/tissue, (C, G) neural induction, and (D, H) rosette emergence plus (E, I) representative immunostaining. Quantification of Day 5 lumbar spinal RosetteArrays with 0.1% DMSO at varied seeding density for (J) cells/tissue, (K) neural induction, and (L) rosette emergence plus (M) representative immunostaining. Dose-response curves for manually and RosetteDetect quantified FB RosetteArray assays of (N) Aspirin, (O) Permethrin, and (P) Rotenone. Each data point represents an average across 2-4 technical replicates with n=40 analyzed tissues per well. Scale bars are 100 µm. Significance in dot plots assessed using 1-way ANOVA with Tukey-Kramer post-hoc analysis, * $p \leq 0.05$. Dose-response curves compared using three-parameter non-linear regression models. If curves are statistically equivalent, then only one curve is displayed.

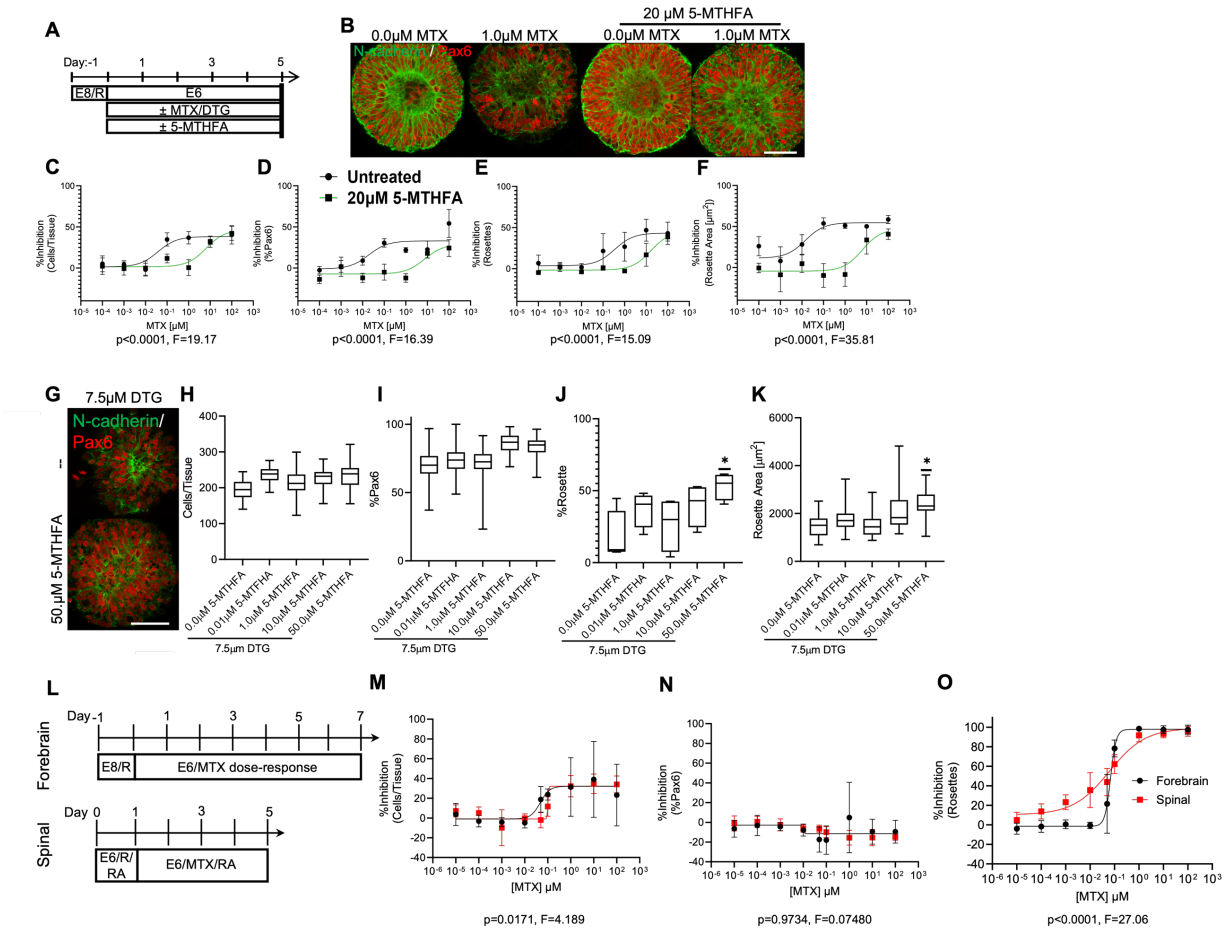

Figure 6. FB and SC RosetteArrays detect folate metabolic pathway-specific risk with regional differences. (A) Culture schema for MTX/DTG exposure with 5-MTHFA rescue in 12-well FB RosetteArrays. (B) Inhibitory effect of 1.0 μM MTX on FB rosette emergence and rescue using concurrent 20.0 μM 5-MTHFA treatment. Quantification of MTX dose-response on 12-well FB RosetteArray derivation with 20.0 μM 5-MTHFA treatment across (C) cells/tissue, (D) neural induction, (E) single rosette emergence, and (F) rosette area metrics. Quantification of DTG's inhibitory effects on 12-well FB RosetteArray derivation with increasing 5-MTHFA supplementation across (H) cells/tissue, (I), neural induction, (J) single rosette emergence, and (K) rosette area metrics. (L) Culture schema for MTX dose-response comparison between 96-well FB and lumbar SC RosetteArrays. Dose-response curves of %inhibition of (M) cells/tissue (N) neural induction, and (O) single rosette emergence. (C-F, H-K) Each data point is the average of technical triplicate, n=50 tissues analyzed per well. (C-F) Three-parameter non-linear regression used to model and compare each metric. (H-K) Significance assessed using 1-way ANOVA with Tukey-Kramer post-hoc analysis, * $p \leq 0.05$. (M-O) Each data point is the average of two biological replicates, each dose in technical quadruplicate, n=40 tissues analyzed per well. Four-parameter non-linear regression used to model and compare each metric. If curves are statistically equivalent, then only one curve is displayed. Scale bars are 100 μm.

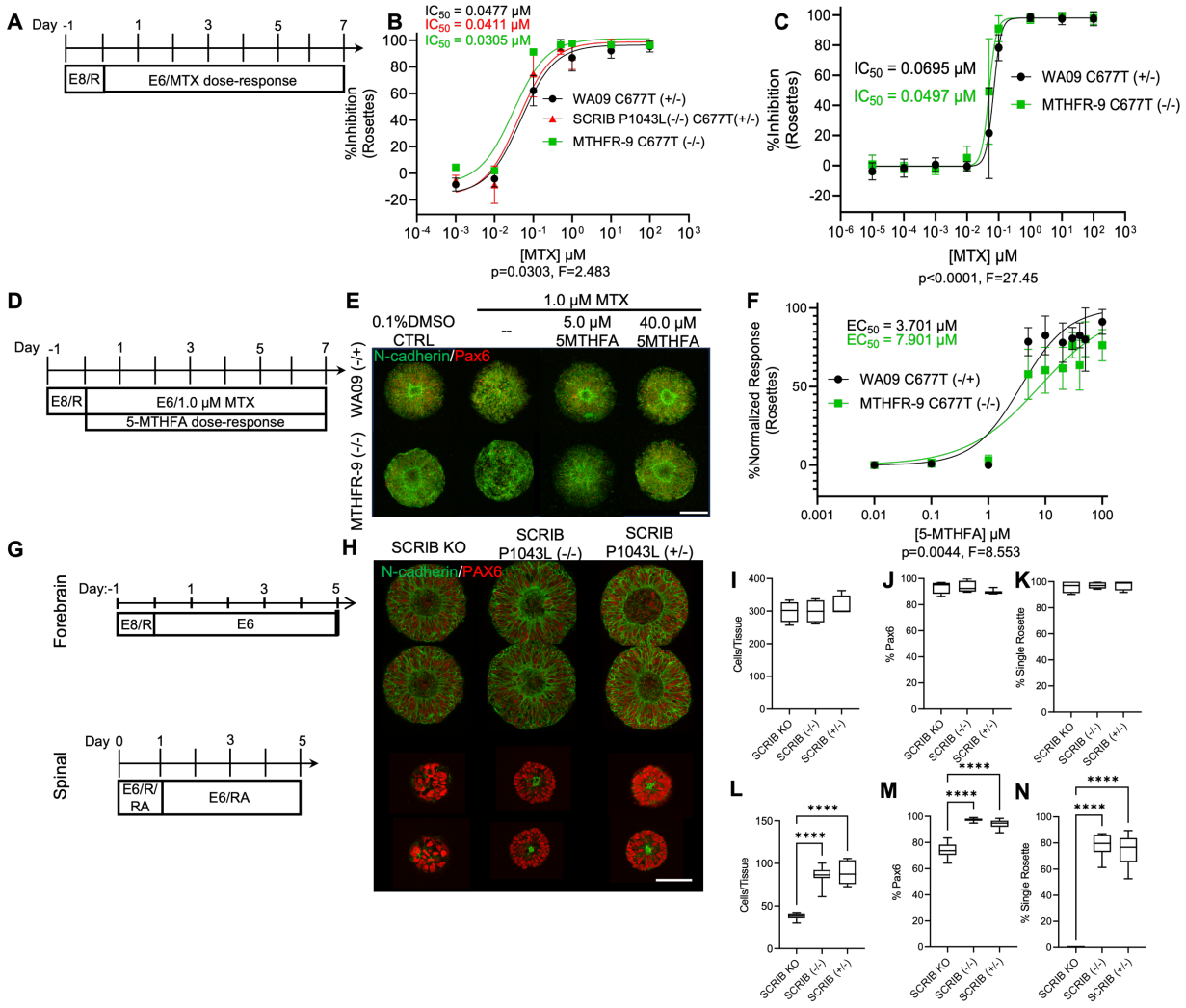

Figure 7. RosetteArrays detect clinically relevant genetic and multifactorial NTD risks. (A) Culture schema for (B) initial and (C) secondary FB RosetteArray MTX dose-response comparison of single rosette emergence across *MTHFR*$^{C677T(-/-)}$ and SCRIB$^{P1043L(-/-)}$/*MTHFR*$^{C677T(+/-)}$ mutant lines and the WA09 *MTHFR*$^{C677T(+/-)}$ isogenic control. (D) Culture schema for 5-MTHFA dose-response rescue of *MTHFR*$^{C677T(-/-)}$ mutant and the WA09 *MTHFR*$^{C677T(+/-)}$ isogenic control under 1 μM MTX exposure with (E) representative staining and (F) quantification of %normalized single rosette emergence. Each data point on a dose-response curve is the average of technical quadruplicate, n=40 tissues analyzed per well. Four-parameter non-linear regression used to model and compare each metric. (G) Culture schema for FB and cervical SC RosetteArrays of SCRIB$^{P1043L(+/-)}$, SCRIB$^{P1043L(-/-)}$, SCRIB^{KO} mutant lines with (H) representative immunostaining and FB (I-K) and SC (L-N) quantification for cells viability/proliferation, neural induction, and %single rosette emergence. Data represents two biologic replicates with n=6-7 technical replicates total. Data is compared via a 1-way ANOVA with Tukey-Kramer post-hoc analysis. **** $p \leq 0.0001$. Scale bars are 100 μm.